Title

Mammalian hybrid pre-autophagosomal structure HyPAS generates autophagosomes

Authors

Kumar, Suresh
Javed, Ruheena
Mudd, Michal
et al.

Mammalian hybrid pre-autophagosomal structure HyPAS generates autophagosomes

Suresh Kumar[1,2], **Ruheena Javed**[1,2], **Michal Mudd**[1,2], **Sandeep Pallikkuth**[3], **Keith A Lidke**[3], **Ashish Jain**[4], **Karthikeyan Tangavelou**[1,2], **Sigurdur Runar Gudmundsson**[5], **Chunyan Ye**[6], **Tor-Erik Rusten**[4], **Jan Haug Anonsen**[7], **Alf Håkon Lystad**[4], **Aurore Claude-Taupin**[1,2], **Anne Simonsen**[4], **Michelle Salemi**[8], **Brett Phinney**[8], **Jing Li**[9], **Lian-Wang Guo**[9], **Steven B Bradfute**[6], **Graham S Timmins**[1,10], **Eeva-Liisa Eskelinen**[11], **Vojo Deretic**[1,2,12]

[1]Autophagy Inflammation and Metabolism Center, University of New Mexico Health Sciences Center, Albuquerque, NM, USA

[2]Molecular Genetics and Microbiology, University of New Mexico Health Sciences Center, Albuquerque, NM, USA

[3]Physics & Astronomy, University of New Mexico, Albuquerque, NM, USA

[4]Faculty of Medicine, University of Oslo, Oslo, Norway.

[5]University of Iceland, Reykjavík, Iceland.

[6]Center for Global Health, University of New Mexico Health Sciences Center, Albuquerque, NM, USA

[7]Biosciences, University of Oslo, Oslo, Norway

[8]Proteomics Core, University of California, Davis, CA, USA

[9]Surgery, University of Virginia, Charlottesville, VA, USA

[10]School of Pharmacy, University of New Mexico Health Sciences Center, Albuquerque, NM, USA

[11]Institute of Biomedicine, University of Turku, Turku, Finland

[12]Lead contact

SUMMARY

The biogenesis of mammalian autophagosomes remains to be fully defined. Here we used cellular and in vitro membrane fusion analyses to show that autophagosomes are formed from a hitherto

unappreciated hybrid membrane compartment. The autophagic precursors emerge through fusion of FIP200 vesicles, derived from the cis-Golgi, with endosomally derived ATG16L1 membranes to generate a hybrid pre-autophagosomal structure, HyPAS. A previously unrecognized apparatus defined here controls HyPAS biogenesis and mammalian autophagosomal precursor membranes. HyPAS can be modulated by pharmacological agents whereas its formation is inhibited upon SARS-CoV-2 infection or by expression of SARS-CoV-2 nsp6. These findings reveal the origin of mammalian autophagosomal membranes, which emerge via convergence of secretory and endosomal pathways, and show that this process is targeted by microbial factors such as coronaviral membrane modulating proteins.

In Brief

Insights into the origin of mammalian autophagosomal membrane and its inhibition by SARS-CoV-2

Graphical Abstract
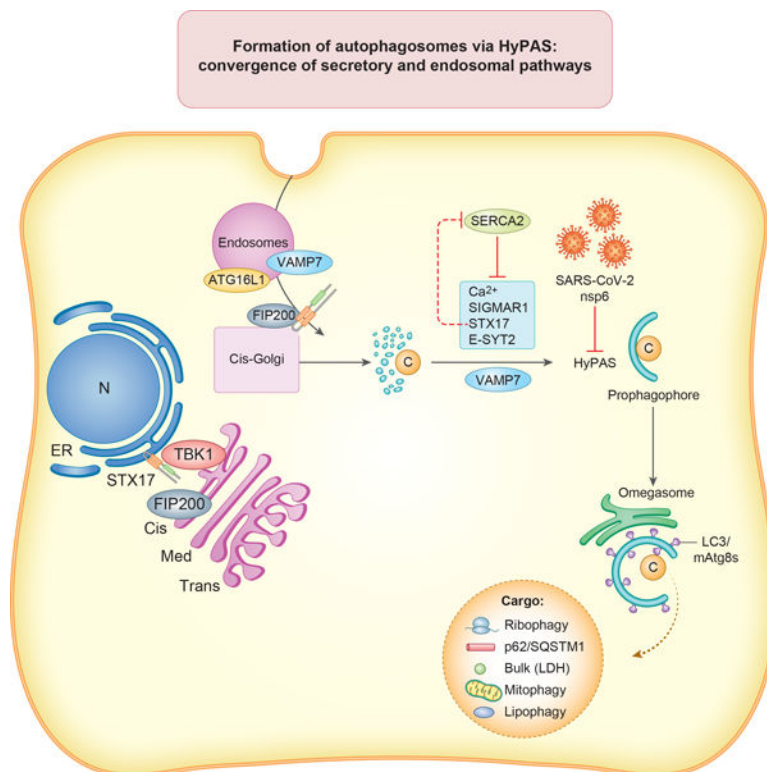
INTRODUCTION

Autophagy is a fundamental biological process contributing to cytoplasmic quality control and cellular metabolism (Deretic and Kroemer, 2021; Levine and Kroemer, 2019; Mizushima et al., 2011) with implications in cancer, infection, metabolic disorders, aging, and neurodegeneration (Deretic, 2021; Klionsky et al., 2021; Levine and Kroemer, 2019). The mammalian autophagy pathway induced by starvation (Morishita and Mizushima, 2019)

is controlled by several protein modules (Morishita and Mizushima, 2019). This includes the FIP200 complex with ULK1/2 kinase acting as the conduit for regulation by mTOR and AMPK, and a protein lipidation system which includes ATG16L1 and results in membrane association of mammalian Atg8 proteins (mAtg8s), such as the autophagosomal marker LC3B (Morishita and Mizushima, 2019). Autophagosomes are presumed to originate from pre-existing membranes contributed by a number of putative sources (Melia et al., 2020). Through subsequent stages, mammalian autophagosomes enlarge, envelop cargo, and merge with lysosomes (Itakura et al., 2012; Matsui et al., 2018b; Reggiori and Ungermann, 2017) whereby the cargo is degraded.

Mammalian systems controlling autophagy include less understood but important contributors, extended synaptotagmins (E-SYTs) (Nascimbeni et al., 2017), and sigma receptor 1 (SIGMAR1) (Yang et al., 2019). E-SYTs function as Ca^{2+}-regulated tethers between endoplasmic reticulum (ER) and plasma membrane (PM) and participate in intermembrane lipid transfer (Saheki et al., 2016). They localize to ER (Saheki et al., 2016; Sclip et al., 2016), PM (Giordano et al., 2013; Min et al., 2007) and membranes with ATG16L1 and LC3 (Nascimbeni et al., 2017). E-SYT2 affects autophagosome biogenesis by regulating phosphatidylinositol-3-phosphate (PI3P) synthesis at the ER-PM contact sites (Nascimbeni et al., 2017). SIGMAR1, an ER resident protein and Ca^{2+}-regulator participating in autophagy (Christ et al., 2019; Vollrath et al., 2014; Yang et al., 2019), is a trimeric transmembrane ER protein (Schmidt et al., 2016) with many physiological effects, including Ca^{2+} transactions at ER-mitochondria contacts (Hayashi and Su, 2007). SIGMAR1 has roles in cancer (Vilner et al., 1995) and neurodegeneration including Alzheimer's disease (Feher et al., 2012) and amyotrophic lateral sclerosis (Vollrath et al., 2014; Watanabe et al., 2016). SIGMAR1 interacts with SNAREs implicated in autophagy, STX17 and VAMP8, and with ATG14L (Yang et al., 2019), a component of PI3KC1 involved in autophagy initiation (Baskaran et al., 2014; Chang et al., 2019). SIGMAR1 interacts with SARS-CoV-2 nsp6 (Gordon et al., 2020) and is a target for pharmacological agents such as chloroquine (CQ) (Gordon et al., 2020; Hirata et al., 2011; Schmidt et al., 2016).

A key area of interest in autophagy research is the integration of known protein complexes with the provenance and source of membranes for autophagosome formation and growth (Hamasaki et al., 2013; Lamb et al., 2013; Melia et al., 2020; Moreau et al., 2011; Nishimura et al., 2017). Here we show that FIP200 and ATG16L1 reside on two distinct sources of membranes, cis-Golgi and PM-derived endosomes respectively, which merge to form autophagosomes. This is a pivotal event leading to the formation of hybrid pre-autophagosomal structures (HyPAS) during autophagosomal biogenesis. Further, HyPAS is a hitherto unknown cellular target perturbed by SARS-CoV-2, positioned at the crossroads between autophagy and the biogenesis of specialized coronavirus-induced compartments (Cottam et al., 2011; Cottam et al., 2014; Fung and Liu, 2019; Gassen et al., 2019; Ghosh et al., 2020; Reggiori et al., 2010).

RESULTS

FIP200 and ATG16L1 compartments merge during autophagy

To test whether FIP200 and ATG16L1 compartments fuse during autophagy induction, we employed a panel of techniques. Confocal microscopy and high content microscopy (HCM) quantification showed overlaps between FIP200 and ATG16L1 compartments, which increased upon autophagy induction by starvation (EBSS) using antibodies against endogenous proteins (Figure 1A,B). Similar results were observed with FIP200 and FLAG-ATG16L1 profiles in HeLa cells (Figures 1C and S1A) and in primary human bronchial epithelial cells (Figure S1B,C).

In full medium, FIP200 displayed mostly perinuclear Golgi localization (Figure S1A) (Kumar et al., 2019) and localized with the cis-Golgi marker GM130 (Figure S1D–F). Upon starvation-induced autophagy FIP200$^+$GM130$^+$ puncta did not increase in abundance (Figure S1E,F) but dispersed from their usual perinuclear location of the Golgi (Figure S1G–I) increasing the number of punctate FIP200 profiles (Figure S1J,K).

ATG16L1 profiles increased in cells induced for autophagy (Figure S1L,M), with a subset of FLAG-ATG16L1 colocalizing with both FIP200 and GM130 (Figure S1N). The % of FIP200 profiles positive for FLAG-ATG16L1 increased upon starvation-induced autophagy (Figure S1A) as quantified by HCM (Figures 1C, S1O). This was confirmed with endogenous FIP200 and ATG16L1 (Figure S1 P,Q), and in another cell line, Huh7 (Figures S1R,S), indicating merger of FIP200 and ATG16L1 profiles during autophagy induction.

By CLEM ultrastructural analysis, this compartment appeared as a combination of vesicular and cisternal profiles, observed most distinctly in the vicinity of both lipid droplets (Figure 1D, subpanels i-iii) and unclosed autophagosomes (Figure 1D, subpanels iv-vii). In EM serial sections, the yellow fluorescence surrounding lipid droplets (corresponding to GFP-FIP200 and mCherry-ATG16L1), appeared morphologically as groups of vesicular (40–55 nm in diameter; Figure 1D, white arrows) and cisternal (Figure 1D, gray arrows) structures of varying sizes and sometimes bent shapes. The morphologically distinct phagophore in Figure 1D (subpanels iv-vii; traced in vii) overlapped with the yellow fluorescence corresponding to the phagophore membrane and was on a cradle of ER in the vicinity of a mitochondrion with potential ER-mitochondrion contact. We interpret the CLEM results as an indication that FIP200-ATG16L1 compartments coincide with vesicular and cisternal profiles in the vicinity of membranous profiles surrounding lipid droplets or are parts of standalone nascent phagophores.

Fluorescently labeled cholera toxin B (CtxB) has been used as a probe to define the ATG16L1$^+$ endosomal compartments derived from PM that participate in autophagosome formation (Ravikumar et al., 2010). We used CtxB-Alexa Fluor 488 (CtxB-488) to detect mixing of cis-Golgi-derived FIP200 and endosomal ATG16L1 compartments. As with ATG16L1 puncta (Figure S1L,M), CtxB profiles increased during starvation (Figure S1T,U). The number of CtxB-488$^+$ profiles that were simultaneously positive for FIP200 and ATG16L1 increased upon autophagy induction (Figures S1V–X) paralleled by increases in % of CtxB-488$^+$ profiles positive for FIP200 (Figure S1Y,Z) or FLAG-ATG16L1 (Figure

S1A[1],B[1]). Several endosomal sub-compartments contribute to ATG16L1 autophagosome precursors, including ATG9A vesicles (Moreau et al., 2011; Puri et al., 2013). ATG9A[KO] cells showed increased basal colocalization between FIP200 and FLAG-ATG16L1, but no further increase upon starvation (Figure S1C[1],D[1]), suggesting that ATG9A affects the flow of membranes to these compartments. In summary, cis-Golgi-derived FIP200 and ATG16L1 originating from PM-derived endosomes, merge during autophagy.

STX17 is required for a merger between FIP200 and ATG16L1 compartments during autophagy induction

STX17 is a SNARE first thought to play a role in autophagosome-lysosome fusion (Itakura et al., 2012) but other studies (Arasaki et al., 2018; Hamasaki et al., 2013; Kumar et al., 2019; Sugo et al., 2018) suggest that STX17 may act earlier in the pathway around initiation stages, consistent with STX17-ATG14L interactions (Diao et al., 2015) and ATG14L's function during initiation (Baskaran et al., 2014; Mizushima et al., 2011). STX17 influences FIP200-containing initiation complexes (Kumar et al., 2019). We tested whether STX17 affects the merger of FIP200 and ATG16L1 compartments by quantifying colocalization of FIP200 and FLAG-ATG16L1 profiles in STX17 KO (STX17[HeLaKO]) (Kumar et al., 2018) vs STX17[HeLaWT] cells. STX17 was required for fusion of FIP200 and FLAG-ATG16L1 compartments (Figures 1E,F and S2A,B). An siRNA knockdown of STX17 reduced overlap between FLAG-ATG16L1 and FIP200, a phenotype that was complemented by siRNA-insensitive mouse Stx17 (Figure S2 C,D). GFP-STX17 colocalization with FLAG-ATG16L1 and FIP200 increased upon autophagy induction (Figure S2 E,F). In STX17[HeLaKO] cells, the area of FLAG-ATG16L1 punctate profiles increased upon autophagy induction (Figure S2G,H), reflecting precursor accumulation. Since STX17 is required for FIP200 peripheral profiles (Kumar et al., 2019), the number of FIP200 puncta was reduced in STX17[HeLaKO] cells. ATG16L1 profiles increased in positivity for the endosomal marker transferrin receptor (TFRC) (Figure S2I,J). The defect in fusion was confirmed in a different cell line (Huh7) (Gu et al., 2019): STX17[Huh7KO] showed no response to starvation whereas in STX17[Huh7WT] cells the % of FIP200^{+} ATG16L1[+] profiles increased (Figures 1G and S2K). Super-resolution microscopy (Figure 1H,I) and cluster quantification showed that FIP200 and FLAG-ATG16L1 were dispersed in STX17[HeLaKO] vs STX17[HeLaWT] cells (Figure 1I). Thus, STX17 is a SNARE contributing to the merger of FIP200 and ATG16L1 compartments.

FIP200 and ATG16L1 compartments undergo membrane fusion

One hypothesis that emerged from the above studies is that FIP200 and ATG16L1 represent two precursor membranes with STX17 facilitating heterotypic fusion between them early in autophagy. To test this, we used an established assay for in vitro membrane fusion (Matsui et al., 2018a; Moreau et al., 2011; Puri et al., 2013; Wang et al., 2017). This method mixes vesicles from different cells expressing green (GFP-FIP200) and red (mCherry-ATG16L1) markers and after addition of an ATP and ATP-regenerating system vesicle fusion is monitored by fluorescence microscopy. We adapted this to permit HCM quantification allowing highly powered analyses and termed it IvitHC (in vitro fusion high content assay) (Figure 2A). ATP-dependent fusion between GFP-FIP200 and mCherry-ATG16L1 vesicles peaked 1h after autophagy induction (Figure S2L,M), resulting in an

8-fold merger of GFP-FIP200 and mCherry-ATG16L1 in wt cells, whereas in STX17^{HeLaKO} fusion was diminished (Figure 2B,C). Thus, STX17 is required for formation of a hybrid pre-autophagosomal structure (HyPAS) observed both in vivo and in vitro.

To confirm that membrane fusion occurs, we developed an assay for content mixing between the two compartments termed <u>p</u>roximity-<u>b</u>iotinylation <u>m</u>embrane-content <u>m</u>ixing assay (PBMM) (Figure 2D). PBMM consists of an integral membrane protein target in one ('donor') compartment and APEX2-fused to a different membrane protein in the partner ('acceptor') compartment (Figure 2D). If the two membranous compartments fuse, either protein can diffuse through the delimiting membrane of the hybrid structure, and proximity biotinylation can occur. If the membranes are just tethered but not fused, the two membranes stay separated and APEX2-has no or very limited access to the target protein. To provide additional layer of control, we combined PBMM with the RUSH system (Boncompain et al., 2012), which is based on a 'hook' and a 'reporter' (Figure 2D). The 'hook' acts as a clamp and keeps the 'reporter" transmembrane protein in the ER (based on streptavidin-streptavidin binding protein/SBP cassette integrated into the transmembrane protein). Only upon breaking the hook-reporter interaction, which is sensitive to biotin, is the reporter free to traffic to its normal intracellular location. We employed the characterized ManII-reporter and an ER hook, which allowed us to control location of ManII in the cell: only after adding biotin did ManII relocate to cis-Golgi (Figure S2N) and colocalized with FIP200 (Figure S2O).

The 'acceptor' compartment in the PBMM system consisted of APEX2-TFRC, with APEX2 facing the cytosol. Target biotinylation (ManII) can occur only after the two compartments fuse allowing ManII and TFRC to come in proximity by diffusion. ManII was biotinylated (assessed by enrichment on avidin beads followed by immunoblotting) in cells co-expressing APEX2-TFRC only after release of the RUSH clamp and was enhanced by starvation, but only in STX17^{WT} and not STX17^{KO} cells (Figure 2E,F). A knockout of FIP200 in HeLa cells reduced starvation-induced mixing of the two compartments (Figure 2G,H). For comparison, we tested the effects of RUBCN. RUBCN is required for LC3 lipidation on noncanonical single membrane structures but is not required for double membrane canonical autophagy (Martinez et al., 2015). Knocking out RUBCN affected neither starvation-induced membrane mixing (Figure S2P) nor HyPAS formation (Figure S2Q,R). Thus, the starvation-induced mixing between cis/early-Golgi compartments (ManII) and endosomal compartments (TFRC) required FIP200, a component of the canonical autophagy core complex transducing signals from mTOR and AMPK upon starvation-induced autophagy.

Relationship of HyPAS to other steps of the autophagy pathway

We tested whether HyPAS is on the pathway for downstream ATG-dependent processes of canonical autophagy or noncanonical pathways (Galluzzi and Green, 2019) such as LC3-associated phagocytosis (LAP) (Martinez et al., 2015; Sanjuan et al., 2007) and LAP-like processes (Fletcher et al., 2018; Heckmann et al., 2019; Jacquin et al., 2017). Comparing STX17^{HeLaKO} and STX17^{HeLaWT} cells, we detected no effects of STX17 KO on increase in LC3-ATG16L1 overlap, as a measure of LAP-like noncanonical autophagy (Fletcher et al., 2018; Jacquin et al., 2017) in response to monensin (Figure S2S,T).

We next used early markers of autophagy initiation, phosphatidylinositol synthase (PIS) (Nishimura et al., 2017) and DFCP1 (Axe et al., 2008). STX17 KO prevented starvation-induced greater colocalization between endogenous FIP200 and mCherry-PIS (Figure S3 A–C). DFCP1 marks omegasomes, membranous structures found in the proximity of LC3 profiles believed to act as a cradle for nascent autophagosomes (Axe et al., 2008; Tooze and Yoshimori, 2010). DFCP1 kinetically segregated from HyPAS and appeared later than HyPAS (Fig S3D,E). HyPAS formation preceded WIPI2b (Dooley et al., 2014) but eventually became positive for WIPI2b (Figure S3F,G). HyPAS appearance preceded LC3$^+$ stage by 15 min (Figure S3H,I) with delayed recruitment of LC3 to HyPAS 30 min after autophagy induction. This makes HyPAS a prophagophore. Double positive LC3$^+$ FLAG-ATG16L1$^+$profiles were reduced in STX17^{KO} cells (Figure S3J–L). HyPAS was independent of the six mATG8s inactivated in Hexa^{KO} cells (Nguyen et al., 2016) (LC3A, LC3B, LC3C, GABARAP, GABARAPL1 and GABARAPL2) which showed normal HyPAS formation (Figure S3M,N). We conclude that HyPAS formation through STX17-dependent heterotypic fusion of FIP200 and ATG16L1 vesicles affects other known events during autophagy initiation.

FIP200-ATG16L1 complexes depend on STX17

FIP200 and ATG16L1 form protein complexes (Fujita et al., 2013; Gammoh et al., 2013; Nishimura et al., 2013). Does formation of these complexes need fusion of precursor membranes? When we compared the ability of endogenous FIP200 and FLAG-tagged ATG16L1 to form protein complexes in HeLa^{WT} vs. STX17^{KO}cells, STX17 was absolutely required (Figure 3A,B) confirmed with endogenous proteins (Figure S3O).

We examined the distribution of endogenous ATG16L1 and FIP200 by cell membrane fractionation. In cells induced for autophagy by starvation, a membranous compartment with ATG16L1 and FIP200 was formed (HyPAS) (Figure S3P, left panel). At least a portion of this compartment contained LC3-II, a downstream autophagosomal marker. HyPAS membranes were enhanced in intensity in cells induced for autophagy (EBSS) relative to fed cells (Figure S3P). This compartment did not form in STX17^{KO} cells (Figure S3Q, right). Instead, in STX17^{KO} cells ATG16L1 and FIP200 floated in a very light membranous neo-compartment, in addition to FIP200 being retained in heavy fractions together with the Golgi marker GM130 (Figure S3Q).

SNARE complexes controlling HyPAS formation

Proteomic analyses with STX17 (Kumar et al., 2019) revealed two R-SNAREs, VAMP7 and VAMP8 as STX17 interactors (Figure 3C), in keeping with prior work (Wang et al., 2016). VAMP8 is implicated in autophagosome-lysosome fusion (Itakura et al., 2012). VAMP7's role is less clear albeit it is implicated in autophagy initiation via ATG16L1 vesicles (Moreau et al., 2011). Under basal conditions, VAMP7 associated with ATG16L1 but not with FIP200 in Co-IPs whereas STX17 associated with FIP200 (Figure 3D,E). In cells induced for autophagy, FLAG-STX17 and endogenous VAMP7 colocalized (Figure S3R). VAMP7 colocalized with HyPAS in starved cells (Figure S3S). Knocking down (KD) VAMP7 reduced the formation of HyPAS (Figure 3F,G and S3 T,U) while KD of VAMP8 did not (Figure S4A,B). We tested in vitro the effects of VAMP7 on HyPAS formation by

IvitHC and found reduced HyPAS formation using vesicles from VAMP7 KD cells (Figure 3H–J). Thus, VAMP7 contributes to early stages of autophagosome formation via fusion of FIP200$^+$ and ATG16L1$^+$ precursor membranes.

Proteomic analyses with STX17 (Figure S4C) showed that it interacts with the Q_{bc} SNARE SNAP-47 in addition to its well characterized Q_{bc} partner SNAP-29 (Diao et al., 2015; Itakura et al., 2012; Takats et al., 2013; Wang et al., 2016). GFP-SNAP-47 colocalized with FLAG-STX17 (Figure S4D). SNAP-47 co-IPed with STX17 but not with STX17 lacking its SNARE domain (Figure S4E,F). KD of SNAP-29 did not affect HyPAS formation (Figure S4G), suggesting that this Q_{bc} SNARE, which acts in autophagosome-lysosome fusion (Diao et al., 2015; Itakura et al., 2012; Takats et al., 2013; Wang et al., 2016) does not participate in HyPAS formation. We could not achieve KD of SNAP-47, to rule in or out this particular SNARE.

Phosphorylation of STX17 directs R-SNARE partnering during HyPAS formation

STX17 is phosphorylated by TBK1 at S202 and this is important in formation of mammalian pre-autophagosomal structures (Kumar et al., 2019). We tested whether TBK1 affected HyPAS formation. TBK1^{KO} HeLa cells (Kumar et al., 2019) had reduced HyPAS formation (Figure 3 K,L). VAMP7 but not VAMP8 lost binding to a non-phosphorylatable mutant (S202A) of STX17 (Figures S4H–K). Complementation of STX17^{KO} cells with WT STX17 or with its phosphomimetic mutant STX17^{S202D} rescued HyPAS formation, whereas the non-phosphorylatable STX17^{S202D} mutant did not (Figure 3M and S4L). Thus, phosphorylation of STX17 and its kinase TBK1 regulate the specificity of STX17 interactions with its R-SNARE partners during HyPAS formation.

SERCA2 is an STX17 partner and Ca^{2+} affects HyPAS formation

Mining the mass spectrometry database MS (MSV000083251) deposited for proteomic analyses with GFP-STX17 (Kumar et al., 2019) uncovered that one of STX17's binding partners is the ubiquitous ER calcium pump SERCA2 (Figure 4A) participating in the early stages of autophagosomal biogenesis (Zhao et al., 2017). The interaction between STX17 and SERCA2 was observed with endogenous proteins (Figure 4B) and confirmed in co-IPs between GFP-STX17 and SERCA2 (Figure S4M). FLAG-STX17 colocalized with endogenous SERCA2 (Figure S4N). SERCA2 pumping removes cytosolic Ca^{2+} (MacLennan and Kranias, 2003; Periasamy and Kalyanasundaram, 2007; Vandecaetsbeek et al., 2011), and conceivably STX17-SERCA2 interactions could involve Ca^{2+}. Thus, we tested whether chelating cytoplasmic Ca^{2} with BAPTA-AM affected HyPAS formation. Under starvation-induced autophagy, HyPAS formation was reduced by BAPTA-AM to an extent similar to the effects of STX17 KO, whereas BAPTA-AM did not further affect HyPAS formation in STX17^{KO} cells (Figures 4C,D and S4O,P). A similar effect of chelation by BAPTA was observed by IvitHC (Figure 4E,F). SERCA2 is inhibited by thapsigargin (TG), and so the expected effect of TG would be increased HyPAS formation. In cells treated with TG (Engedal et al., 2013; Ganley et al., 2011), HyPAS formation was increased in basal conditions (Figure 4 G). The effect of TG was abrogated in STX17^{KO} cells (Figures 4 G,H and S4Q,R). SERCA2 expression inhibited HyPAS (Figure 4I). SERCA2 was present in multiple fractions on OptiPrep gradients (Figure S3P). During autophagy induction

(HBSS), cytosolic Ca^{2+} (measured by FLUO-3) was elevated (Figure 4J,K), as described (Cardenas et al., 2010). In STX17[KO] cells, cytosolic calcium did not increase, consistent with unabated activity of SERCA2 in the absence of its partner STX17 (Figure 4J,K). We conclude that STX17 interacts with SERCA2 and that STX17 directly or indirectly inhibits its function (Figure 4L) during autophagy induction.

E-SYT2, an STX17 interactor, affects HyPAS formation

Among other potential interactors of STX17 based on the MS (MSV000083251) database we identified E-SYT2 as an STX17 partner (Figure 5A). E-SYT2 is a member of the ESYT family of ER proteins with a role for Ca^{2+} in tethering to PM (Giordano et al., 2013; Min et al., 2007; Saheki et al., 2016). Interactions between STX17 and E-SYT2 were observed with endogenous proteins (Figure 5B) and confirmed in co-IPs (Figure S5A). FLAG-STX17 and GFP-E-SYT2 profiles overlapped by immunofluorescence (Figure 5C). FLAG-E-SYT2 colocalized with HyPAS (Figure S5B). E-SYT2-KD prevented HyPAS formation (Figure S5C-E) indicative of fusion arrest by the juxtaposition of ATG16L1 and FIP200 profiles (Figure S5C) similar to the STX17 KO effects (Figure 1E).

E-SYT2[KO] cells (Saheki et al., 2016) displayed juxtaposition of ATG16L1 and FIP200 profiles (Figure 5D and S5F), with no HyPAS formation (Figure 5E,F) upon autophagy induction (EBSS). E-SYT2 was necessary for in vitro HyPAS formation by IvitHC (Figure 5G,H). E-SYT2 was required for mixing of cis-Golgi and endosomal compartments in the PBMM assay (Figure 5 I,J). Finally, E-SYT2 was important for HyPAS formation in response to SERCA inhibition by TG (Figure S5G,H), suggesting that it acts as a downstream effector of SERCA and Ca^{2+}. Thus, in addition to SERCA, which regulates cytosolic Ca^{2+}, E-SYT2, which can act as an effector of Ca^{2+} (Giordano et al., 2013; Saheki et al., 2016), controls HyPAS formation.

E-SYTs play a role in membrane tethering at ER-PM contact sites (Giordano et al., 2013; Saheki et al., 2016). Synaptotagmins in principle control SNARE complexes with the paradigm being based on Synaptotagmin 1 (SYT1) (Brose et al., 1992; Chapman, 2002). We thus wondered if E-SYT2 may have an as-yet unrecognized function in HyPAS formation catalyzed by SNAREs. Homology alignments with SYT1 revealed conserved polybasic regions in E-SYT2's C2C domain corresponding to the polybasic region in SYT1's C2B domain (Figure 5K). We mutated six basic residues in E-SYT2, K805, R806, R807, R809, R810, K811A to generate E-SYT2[6A]. The corresponding polybasic stretch in SYT1 is essential for the regulatory effects of SYT1 on its cognate syntaxin (Brewer et al., 2015). Co-IP analyses showed reduced binding to STX17 of E-SYT2[6A] vs GFP-E-SYT2[WT] (Figure 5L,M). E-SYT2[6A] could not rescue HyPAS formation in E-SYT2[KO,] whereas E-SYT2[WT] did (Figure 5N and S5I). Thus mutational analysis, based on prototypical synaptotagmin-syntaxin relationships, revealed that E-SYT2 interacts with STX17 to regulate its function in HyPAS formation.

We observed reduced levels of STX17 in VAMP7 immunoprecipitates from E-SYT2[KO] cells (Figure 5O,P). Comparing overexpressed GFP-VAMP7 and GFP-VAMP8 in complexes with FLAG-STX17, we observed that in E-SYT2[KO] cells GFP-VAMP7, but not GFP-VAMP8, was diminished in SNARE complexes (Figure 5Q,R). Thus E-SYT2, in addition to its

previously characterized roles in lipid transfer (Saheki et al., 2016) and PI3P production at ER-PM contact sites during peripheral LC3 puncta formation (Nascimbeni et al., 2017), plays a role in early stages of autophagosome formation.

HyPAS depends on SIGMAR1

The STX17 interactors SERCA and STX17 controlling HyPAS formation are located in the ER. Another ER-localized interactor of STX17 is SIGMAR1 (Yang et al., 2019), which plays a role in autophagy (Christ et al., 2019; Vollrath et al., 2014; Yang et al., 2019). SIGMAR1 co-fractionated with HyPAS in OptiPrep density gradients (Figure S3O). HyPAS formation was reduced in SIGMAR1^{KO} cells (Yang et al., 2019) relative to WT cells (Figure 6A–C). FLAG-SIGMAR1 co-IPed with VAMP7 (Figure S5J). Complementation, of SIGMAR1^{KO} with full length FLAG-SIGMAR1 recovered HyPAS formation (Figure 6D,E and S5K). Expression of a truncated version of SIGMAR1, FLAG-SIGMAR1N80 (Yang et al., 2019), consisting of the N-terminal transmembrane domain and only a portion of the cytosolic-facing surface of the SIGMAR1 protomers within the SIGMAR1 trimeric architecture (Schmidt et al., 2016), did not restore HyPAS formation (Figure 6D,E and S5K). This was in keeping with effects on mitophagy (Yang et al., 2019). Thus, the ability of SIGMAR1 to form trimers or to interact with additional components is necessary for HyPAS formation in autophagy.

HyPAS is important for conventional autophagy of diverse cargo

We tested whether E-SYT2 and, by extension, HyPAS are responsible for removal of autophagic cargo. We tested Parkin-dependent mitophagy (Narendra et al., 2008; Youle, 2019) in E-SYT2^{WT} and E-SYT2^{KO} HeLa cells transfected with YFP-Parkin (Narendra et al., 2008), using mtDNA antibody to quantify mitophagy (Gu et al., 2019; Lazarou et al., 2015; Nguyen et al., 2016) by HCM while gating on YFP-Parkin$^+$ cells. E-SYT2^{KO} cells had diminished mitophagy relative to WT elicited with OA (oligomycin+antimycin) (Figure 6F,G) or CCCP (Figure S5L,M). In a complementation assay, E-SYT2^{6A} mutant, which does not bind STX17, failed to restore mitophagy whereas E-SYT2^{WT} did (Figure 6H and S6A). SIGMAR1^{KO} cells transfected with YFP-Parkin showed reduced mitophagy in response to CCCP (Figure S6 B,C). Thus, HyPAS is required for mitophagy.

We next tested autophagy of ribosomes (ribophagy) (An and Harper, 2018; An et al., 2020; Eskelinen, 2008; Tanaka et al., 2000; Wyant et al., 2018). We transfected the RPL28-Keima ribophagy probe (An and Harper, 2018)) into WT and E-SYT2^{KO} HeLa cells. After starvation for 8 h in EBSS, Keima-positive autolysosomal organelles engaged in ribophagy were quantified by HCM (Ex/Em 560/620 nm) (Katayama et al., 2011; Violot et al., 2009). E-SYT2^{KO} cells showed reduced ribophagy relative to E-SYT2^{WT} parental cells (Figure S6D,E). The E-SYT2^{6A} mutant failed to complement ribophagy whereas E-SYT2^{WT} did (Figure S6F,G). SIGMAR1^{KO} 293A cells exhibited reduced ribophagy (Figure 6I and S6H). Thus, HyPAS is important for ribophagy.

We next tested bulk autophagy (Kopitz et al., 1990; Pattingre et al., 2003; Szalai et al., 2015) employing LDH-Keima construct (An and Harper, 2018). E-SYT2^{KO} cells had fewer autolysosomes containing the bulk autophagy probe LDH-Keima (An and Harper, 2018)

relative to E-SYT2^{WT} cells (Figures 6J and S6I), and confirmed in SIGMAR1^{KO} 293A cells (Figures 6K and S6 J).

In response to starvation, E-SYT2KO cells exhibited reduced lipophagy-lipolysis (Zechner et al., 2017) (Figure S6K,L) and degradation of endogenous SQSTM1/p62 (Figure S6M,N), a principal autophagy receptor (Bjorkoy et al., 2005; Pankiv et al., 2007). The starvation-induced degradation of p62 paralleled that of ManII (Figure S6O,P), an early Golgi resident enzyme that colocalizes with FIP200 and was utilized in the PBMM assay (Figure S2O). ManII was degraded during starvation, abrogated in E-SYT2^{KO} cells (Figure S6O,P). Thus, HyPAS is critical for autophagy of diverse cargo.

Phagophores eventually close to sequester cargo. E-SYT2 was required for protection of p62 from proteinase K (Nguyen et al., 2016; Velikkakath et al., 2012), an assay for autophagic sequestration (Figure S6Q,R). ESCRTs catalyze phagophore closure (Takahashi et al., 2018; Zhen et al., 2020). When cells are depleted of the ESCRT-III component CHMP2A, this results in morphologically scorable aberrant retention of the ESCRT-III component CHMP4B (Teis et al., 2008) on unclosed autophagosomes (Zhen et al., 2020). In cells induced for autophagy by starvation, CHMP4B puncta increased upon CHMP2A KD, indicative of accumulating unclosed autophagosomes (Zhen et al., 2020). The CHMP4B puncta were diminished in E-SYT2^{KO} HeLa cells, indicative of fewer phagophores being formed (Fig. S6 S,T).

HyPAS is a target of pharmacological agents

SIGMAR1 is a target of pharmacological agents (Christ et al., 2019; Hayashi and Su, 2007; Hirata et al., 2011; Vollrath et al., 2014) including chloroquine (CQ) (Gordon et al., 2020; Schmidt et al., 2016), an inhibitor of autophagy (Klionsky et al., 2016). CQ neutralizes lysosomes (Klionsky et al., 2016), perturbs Golgi (Mauthe et al., 2018) and binds SIGMAR1 (Gordon et al., 2020; Schmidt et al., 2016). In the IvitHC assay, CQ inhibited HyPAS formation in vitro (Figure S7A,B) while bafilomycin A1 did not (Figure S7A,B). The known CQ target SIGMAR1 was important for STX17 and E-SYT2 interactions (Figure S7C,D) whereas CQ treatment inhibited them (Figure S7E, F). The effect was specific since CQ did not inhibit STX17 and SERCA2 interactions (Figure S7E,G). Thus, CQ interferes with autophagy at a very early point, HyPAS formation.

We next tested other SIGMAR1 ligands implicated in autophagy (Christ et al., 2019; Hirata et al., 2011; Maher et al., 2018; Tesei et al., 2018) for their effects on HyPAS. The agonist cutamesine induced HyPAS formation in cells grown in full medium (Figure S7H,I) whereas the antagonist BD1047 inhibited HyPAS formation induced by starvation (Figure S7J,K). Thus, pharmacological agonists and antagonists of SIGMAR1 affect the formation of the precursor structure to mammalian autophagosomes.

SARS-CoV-2 infection and SARS-CoV-2 nsp6 target and inhibit HyPAS

Autophagy intersects morphologically with coronavirus biogenesis (Cottam et al., 2011; Cottam et al., 2014; Fung and Liu, 2019; Gassen et al., 2019; Hoffmann et al., 2021; Miao et al., 2021; Reggiori et al., 2010; Schneider et al., 2021). We tested whether HyPAS was targeted during infection employing Huh7 and additionally Calu3 cells, a human cell

line used to study SARS-CoV-2 infection in disease site-relevant context (Hoffmann et al., 2020a; Hoffmann et al., 2020b). Cells were infected with SARS-CoV-2 (USA-WA1/2020) using viral preparations causing cytopathic effect in Vero E6 (Bradfute et al., 2020) and verified in Huh7 cells (Figure S7L). SARS-CoV-2 infection inhibited HyPAS formation in Calu3 (Figures 7A,B) and Huh7 (Figures S7M,N) cells. Thus, HyPAS is affected by SARS-CoV-2.

SARS-CoV Nsp6 causes LC3 puncta to be smaller than regular autophagosomes (Cottam et al., 2014). The SARS-CoV-2 ORF1 polyprotein, which includes nsp6, shows 76% identity to SARS-CoV (Zhou et al., 2020). We carried out proximity biotinylation proteomic analysis with APEX2-SARS-CoV-2-nsp6 in stably transfected (FLIP-IN) cells with APEX2-nsp6 expression controlled by the Tet-ON system (Figure 7C, Table ST1A–C). The functionality of the SARS-CoV2-nsp6 construct was validated in an assay developed for nsp6 of SARS-CoV (Cottam et al., 2014) (Figure S7O). The proteomic data confirmed the previously reported nsp6-SIGMAR1 interaction (Gordon et al., 2020) and revealed that nsp6 interacts with VAMP7, E-SYT2, SERCA2, and TBK1 (Figure 7D, Table ST1B). Interactions between SARS-CoV-2 nsp6 and SERCA2 were validated by co-IP (Figure S7P). In summary, proximity biotinylation proteomic analysis uncovered ESYT2, VAMP7, and SERCA2 as SARS-CoV-2 nsp6 interactors, and revealed that the HyPAS regulator TBK1, which phosphorylates STX17 (Kumar et al., 2019) and authorizes it to engage VAMP7, is targeted by SARS-CoV-2 nsp6.

We next tested whether SARS-CoV-2 nsp6 affects HyPAS. Following published procedures (Cottam et al., 2014), we expressed SARS-CoV-2 nsp6 in HeLa cells and quantified HyPAS formation by HCM. SARS-CoV-2 nsp6 (GFP-nsp6) reduced HyPAS yields upon autophagy induction (EBSS) (Figures 7E and S7Q,R). In contrast to nsp6, expression of SARS-CoV-2 ORF3a, reported to interfere with autophagosomal fusion with lysosomes (Miao et al., 2021), or ORF8 did not significantly inhibit HyPAS formation (Figures 7F,G and S7S,T).

To test the effects of nsp6 in vitro by IvitHC, we co-expressed FLAG-nsp6 with GFP-FIP200 and separately co-expressed FLAG-nsp6 with mCherry-ATG16L1 in HeLa cells before preparing vesicles for in vitro fusion (Figure 7H). IvitHC showed that nsp6 inhibited HyPAS formation in vitro (Figure 7I,J). Thus, SARS-CoV-2 nsp6 interferes with early formation of autophagosomes at the HyPAS stage.

DISCUSSION

We have identified a critical step in the biogenesis of canonical autophagosomes in mammalian cells. This step is embodied in HyPAS, a prophagophore compartment formed through fusion of membranes derived from the constitutive secretory pathway and the endosomal pathway (Fig 7K). The system responds to starvation, a classical inducer of autophagy, and engages ATG16L1-positive endosomal vesicles (Lystad et al., 2019; Moreau et al., 2011; Ravikumar et al., 2010; Travassos et al., 2010), which fuse with FIP200-positive ER/Golgi-derived membranes. Thus, mammalian cells commit to autophagy through a regulated intermixing of two membrane sources that are normally not intended to directly

communicate, one working vectorially within the secretory pathway and the other running in the opposite direction via the endocytic pathway.

The regulation of the FIP200 complex by mTOR (Ganley et al., 2009; Hosokawa et al., 2009; Jung et al., 2009; Kim et al., 2011) and AMPK (Egan et al., 2011; Inoki et al., 2012; Kim et al., 2011), which extends to phosphorylation of ATG16L1 by ULK1 (Alsaadi et al., 2019), integrates metabolic inputs (Deretic and Kroemer, 2021) into HyPAS formation. FIP200 and ATG16L1 connect HyPAS to immunity and inflammation, further extended by TBK1 (Chauhan et al., 2015; Pilli et al., 2012; Ravenhill et al., 2019; Saitoh et al., 2008; Shi et al., 2020; Thurston et al., 2009; Travassos et al., 2010; Vargas et al., 2019; Wild et al., 2011). TBK1 controls STX17 (Kumar et al., 2019), a centerpiece of the HyPAS apparatus.

A long-standing question in mammalian autophagy has been where do the autophagosomal membranes come from? For the most part, two primary origins of mammalian autophagic membranes have been considered: (i) ER-centric (Axe et al., 2008; Hara et al., 2008; Hayashi-Nishino et al., 2009; Itakura and Mizushima, 2010, 2011; Mizushima et al., 2011; Nishimura et al., 2017; Tooze and Yoshimori, 2010) or (ii) PM and endosomal-centric (Knaevelsrud et al., 2013; Longatti et al., 2012; Moreau et al., 2011; Puri et al., 2013; Puri et al., 2018; Ravikumar et al., 2010; Soreng et al., 2018). Our study provides the physical and mechanistic link between the two disparate theses and explains how they can both be correct. This accommodates the reported role of ER-Golgi intermediate compartment and COPII vesicles (Ge et al., 2013; Ge et al., 2014) along with the effects of FIP200 (Ge et al., 2017) and the associated tubulovesicular morphology (Hayashi-Nishino et al., 2009). Additional contributors to autophagosomal membranes have been reported (Hailey et al., 2010; Hamasaki et al., 2013; Nascimbeni et al., 2017; Nishida et al., 2009), which may participate at the HyPAS or other stages.

HyPAS is formed via SNARE-dependent fusion centered upon STX17 and is affected by Ca^{2+}. The role of Ca^{2+} along the autophagosomal-autolysosomal continuum is complex and acts as a positive or negative regulator depending on the checkpoint reached: (i) Prolonged Ca^{2+} influx from ER to mitochondria (mitochondria-associated ER-membranes; MAM) (Hayashi and Su, 2007) is necessary to maintain mitochondrial function, and when it is disrupted (Cardenas et al., 2010; Criollo et al., 2007) this induces AMPK and autophagy (Cardenas et al., 2010). (ii) As we show, Ca^{2+} is a positive co-factor for HyPAS formation with all three STX17 partners within the HyPAS apparatus, SIGMAR1 (Hayashi and Su, 2007), E-SYT2 (Saheki et al., 2016), and SERCA2 (MacLennan and Kranias, 2003; Periasamy and Kalyanasundaram, 2007; Vandecaetsbeek et al., 2011) being known regulators or effectors of Ca^2. SIGMAR1 redistributes in response to Ca^{2+} from the MAM to the entire ER (Hayashi and Su, 2007), thus becoming available to participate in HyPAS formation. (iii) Ca^{2+} is a negative regulator of phagophore separation from membranes to which they are initially tethered (Bissa and Deretic, 2018; Zhao et al., 2017). (iv) Pharmacological inhibition of SERCA prevents fusion between autophagosomes and lysosome (Ganley et al., 2011; Mauvezin et al., 2015). Thus, Ca^{2+} transients are necessary to move the autophagy pathway from its beginning to its completion.

STX17 role in HyPAS formation is compatible with studies suggesting that it functions in a number of ways, including autophagic initiation (Kumar et al., 2019) at mitochondria-ER contact sites (Arasaki et al., 2018; Hamasaki et al., 2013), where another HyPAS component, SIGMAR1 operates (Hayashi and Su, 2007). Prior studies (Diao et al., 2015; Guo et al., 2014; Itakura et al., 2012; Takats et al., 2013; Wang et al., 2016) and recent work (Gu et al., 2019; Kumar et al., 2020; Kumar et al., 2018; Yang et al., 2019) have associated STX17 with autolysosomal biogenesis. The function of STX17 in autophagosome-lysosome fusion as a sole Q_a SNARE has been contested and requires a contribution of additional non-cognate SNAREs such as Ykt6 (Bas et al., 2018; Gao et al., 2018; Matsui et al., 2018b; Takats et al., 2018) and Stx16 (Gu et al., 2019), because STX17 inactivation alone does not prevent autophagic cargo degradation (Gu et al., 2019; Matsui et al., 2018b). STX17 orchestrates progression of the autophagy pathway, whereby different combinations of STX17 and its R-SNARE partners catalyze sequential stages. During HyPAS formation, STX17 favors VAMP7 over VAMP8, which acts in autolysosome formation (Diao et al., 2015; Itakura et al., 2012; Wang et al., 2016; Yang et al., 2019). However, SNARE redundancy or compensation in HyPAS formation is possible.

Autophagy and coronaviruses are intertwined (Cottam et al., 2011; Cottam et al., 2014; Fung and Liu, 2019; Guo et al., 2016; Guo et al., 2017; Ko et al., 2017; Prentice et al., 2004; Reggiori et al., 2010; Zhu et al., 2016)(Schneider et al., 2012; Zhao et al., 2007). Coronaviruses actively remodel cellular membranes and generate protrusion-type viral-replication compartments (VRCs) (Strating and van Kuppeveld, 2017). The coronavirus VRCs include interconnected double membrane vesicles (DMVs), vesicle packets of merged DMVs, additional convoluted membranes (CM), and represent the cellular locales for RNA replication-transcription complexes (RTCs) (EA and Jones, 2019; Knoops et al., 2008; Sola et al., 2015). Some aspects of coronavirus VRCs include morphological features of autophagosomes (e.g. DMVs) (Snijder et al., 2006) and engage peripheral autophagy factors TMEM41B and VMP1 (Schneider et al., 2021) but are distinct from classical autophagosomes (Cottam et al., 2014; Reggiori et al., 2010). The inhibition of HyPAS by SARS-CoV-2 nsp6 suggests potential diversion of membrane sources engaged in autophagy toward the formation of DMVs and CMs to support coronavirus RTCs.

Of the three proteins nsp3, nsp4, and nsp6, implicated in coronavirus remodeling of host membranes to generate VRCs (Fung and Liu, 2019; Reggiori et al., 2010) (Angelini et al., 2013; Snijder et al., 2020; Wolff et al., 2020), we focused on nsp6. This was based on nsp6's action alone on LC3 profiles (Cottam et al., 2014), the dearth of nsp3 and nsp4 host protein interactors relative to the rich portfolio of nsp6 partners (Stukalov, 2020), and the specialized engagement of nsp3 and nsp4 in VRCs and DMV pores (Angelini et al., 2013; Snijder et al., 2020; Wolff et al., 2020). Our own proximity biotinylation proteomic analysis (MSV000087840) with SARS-CoV-2 nsp6 indicates multiple interactions between nsp6 and components of the HyPAS fusion apparatus (E-SYT2, VAMP7, SIGMAR1) and regulators of HyPAS formation including SERCA2 (Ca^{2+} pump with Ca^{2+} being a key signal for HyPAS formation), TBK1 (a protein kinase phosphorylating and authorizing STX17 to associate with VAMP7), and a number of key regulators of autophagy, mTOR and AMPK (Table ST1B,C). Conversely, factors controlling fusion processes along the endosomal organelles where ATG16L1 is located, i.e. ORF3a, did not affect HyPAS

formation, indicating that nsp6 domain of action is mostly within the early secretory pathway, albeit we noticed nsp6 interactions with a number of Golgi proteins (Table ST1C).

The definition of HyPAS in this work is of significance not only as a potential target for pharmacological intervention in COVID-19 but is of fundamental value for our understanding of the formation of autophagosomes, and hence for many physiological functions and disease states affected by autophagy.

Limitations of the study

The findings that SARS-CoV-2 nsp6 inhibits HyPAS beckon future studies to discern whether the membranes used for HyPAS are diverted by the virus for its own DMVs. Further studies are needed to rule in or out contributions of nsp3 and nsp4 to HyPAS inhibition, address nsp3, nsp4 and nsp6 interactions, and interactions of nsp6 with multiple components of the HyPAS apparatus. The SARS-CoV-2 effects on HyPAS invite follow-up studies of physiological consequences in infection models or in clinical studies with pharmacological agents. Technical limitations include our inability to demonstrate whether SNAP-47 works in HyPAS formation. We point out that R-SNAREs and other SNARES may act redundantly and compensate individual knockouts.

STAR METHODS

RESOURCE AVAILABILITY

Lead contact information—Further information and requests for resources and reagents should be directed to and will be fulfilled by the lead contact Vojo Deretic (vderetic@salud.unm.edu).

Data and code availability

- The Raw MS DIA/DDA data used in this study have been deposited at the MassIVE proteomics repository https://massive.ucsd.edu MSV000083251and MSV000087840.

- This paper does not report original code.

- Any additional information required to reanalyze the data reported in this paper is available from the lead contact upon request.

EXPERIMENTAL MODEL AND SUBJECT DETAILS

Cell culture—HEK 293T, Huh7 and HeLa cells were obtained from ATCC and maintained in ATCC recommended media. 293T APEX2-nsp6 cells were grown in DMEM supplemented with 10% fetal bovine serum and antibiotic. STX17^{KO} HeLa, FIP200^{KO} HeLa, RUBCN^{KO} HeLa, Hexa^{KO} HeLa, TBK1^{KO} HeLa and STX17^{KO} Huh7, ATG9^{KO} Huh7 cells were cultured in DMEM supplemented with 10% fetal bovine serum and antibiotic as described previously (Gu et al., 2019; Kumar et al., 2019). E-SYT2^{KO} and parental wild type HeLa cells were cultured as described previously (Saheki et al., 2016). HEK293A SIGMAR1^{KO} and parental wild type HEK293A cells were grown as described previously (Yang et al., 2019). Primary NHBE (normal human bronchial epithelial) cells

were obtained from Lonza and cultured in media from Lonza (BEGM™ bronchial epithelial cell growth medium BulletKit™; Catalog #: CC-3170).

Generation of CRISPR mutant cells—STX17 CRISPR in HeLa and Huh7 cells and ATG9 CRISPR in Huh7 were generated as described earlier (Gu et al., 2019; Kumar et al., 2019; Kumar et al., 2018). Briefly, the lentiviral vector carrying both Cas9 enzyme and a gRNA targeting STX17 (GATAGTAATCCCAACAGACC), and ATG9 (GACCCCCAGGAGTGTGACGG) were transfected into HEK293T cells together with the packaging plasmids psPAX2 and pCMV-VSV-G at the ratio of 5: 3: 2. Two days after transfection, the supernatant containing lentiviruses was collected and used to infect the cells. 36 hours after infection, the cells were treated with puromycin (1 mg/ml) for one week to select STX17-knockout cells. The knockouts were confirmed by western blotting. SIGMAR1^KO in HEK293A are described previously (Yang et al., 2019), E-SYT2KO cells are described previously (Saheki et al., 2016).

Generation of 293T Flp-In-nsp6 ^TetON cells—293T Flp-In host cells were transfected with FLAG-APEX2-nsp6 plasmid and the pOG44 expression plasmid at ration of 9:1. After overnight transfection, cells were washed with PBS and fresh medium was added. 48 h after transfection, cells were trypsinized and seeded at 25 % confluency, followed by incubation at 37°C for 8 h. Cells were then supplied with medium containing 100 μg/mL hygromycin and hygromycin-resistant clones were selected. The clones were tested by western blotting. The tested clones incubated in the medium containing 1 μg/mL tetracycline overnight were determined by western blot with FLAG.

METHOD DETAILS

Antibodies and reagents—The following antibodies and dilutions were used: STX17 (Sigma, HPA001204; 1:1000 (WB)); Flag (mouse monoclonal Sigma; F1804, used at 0.5 μg/ml and 1:1,000 for (WB); 1:250 (IF)); GFP (rabbit Abcam; ab290; 0.5 μg/ml IP and 1:4,000 (WB)); LC3 (rabbit; MBL International PM036, 1:500 (IF)); FIP200 (rabbit; Proteintech; 17250–1-AP, 1:200 (IF)); FIP200 (rabbit Cell Signaling Technology; 12436, 1:1000 (WB)); SERCA2 (Mouse ThermoFisher; MA3–919, 1:150 (IF), 1:500 (WB)); ATG16L1 (mouse; MBL International M152–3, 1:200 (IF); ATG16L1 (rabbit; MBL International PM040, 1:1000 (WB); GM 130 (mouse BD Biosciences, RUO-610822, 1:500 (IF); 1:1000 (WB)); mouse anti-DNA antibody (IF:1:200) was purchased from Progen (#61014); VAMP7 (rabbit Cell Signaling Technology; 14811, 1:1000 (WB)); VAMP8 (1:1,000 (WB); rabbit monoclonal; ab76021; Abcam); E-SYT2 (rabbit ThermoFisher PA5–51689, 1:200 (IF), 1:500 (WB)); GRP78/Bip (1:200 (IF); goat polyclonal; sc10086; Santa Cruz Biotechnology, Inc.); Dynabeads Protein G (Thermo Fisher Scientific 10003D 50μl/ IP); Bafilomycin A1 (Baf A1, InvivoGen, 13D02-MM); OptiPrep Density Gradient Medium (Sigma, D1556); Lipofectamine 2000, Thermo Scientific, 11668019; BAPTA-AM, Sigma Aldrich, A1076;BAPTA, Millipore Sigma 196418; Goat anti mouse IRDye 680 (LI-COR, 925–68020);Goat a Rabbit IRDye 800 (LI-COR, 926–32211); Trueblot anti-mouse DyLight 680, (Rockland, 18–4516-32); Trueblot anti-rabbit DyLight 800 (Rockland, 18–8816-31), BODIPY™ 493/503 (4,4-Difluoro-1,3,5,7,8-Pentamethyl-4-Bora-3a,4a-Diaza-*s*-Indacene),

(ThermoFisher D3922); Oleic Acid-Albumin from bovine serum (Millipore SIGMA 03008); Biotinyl tyramide (biotin-phenol) AdipoGen LIFE SCIENCES CDX-B0270-M100.

Plasmid transfections—pDest-GFP-STX17(Kumar et al., 2018), pDest-GFP-STX17^{S202A}, pDest-GFP-STX17^{S202D} (Kumar et al., 2019), pDest-GFP-VAMP8(Kumar et al., 2018) FLAG-ATG16L1 (Chauhan et al., 2016), EGFP-DFCP1(Axe et al., 2008), SIGMAR1-FLAG and SIGMAR1 N80-FLAG (Yang et al., 2019), EGFP-WIPI2b (Bakula et al., 2017) YFP-Parkin (Narendra et al., 2008) have been described earlier. EGFP-hFIP200(Addgene #38192), mCherry-PIS (Addgene # 119078), EGFP-E-SYT2 (Addgene # 66831), GFP-VAMP7 (Addgene #45920), were from Addgene. Keima-RPL28 and LDH-Keima was from Heeseon An and J. Wade Harper (Harvard Medical School, Boston, MA (An and Harper, 2018). SARS-CoV-2-nsp6 was synthesized and cloned into pDest-GFP or pDest-FLAG. E-SYT2^{6A} was mutated using site directed mutagenesis kit using following primers in GFP-E-SYT2 to generate:Fw,CGCATGTATTTATTACCAGACGCCGCCGCCTCAGGAGCCGCCGCCA CACACGTGTCAAG;Rw,CTTTGACACGTGTGTGGCGGCGGCTCCTGAGGCGGCGG CGTCTGGTAATAAATACATGCG. Other plasmids and corresponding mutants used in this study, were cloned into pDONR221 using BP cloning, and expression vectors were made utilizing LR cloning (Gateway, ThermoFisher Scientific) in appropriate pDEST vectors for immunoprecipitation and other assays. Point-mutants were generated using the QuikChange Site-directed Mutagenesis Kit (Agilent, 200523). Plasmid constructs were verified by conventional restriction enzyme digestion and/or by DNA-sequencing. Plasmids were transfected using Lipofectamine 2000 (Thermo Fisher Scientific).

PBMM assay—HeLa ^{WT}, STX17^{KO} and RUBCN^{KO} and Huh7^{WT} and Huh7^{FIP200KO} cells were transfected with Ii-Str-ManII-SBP-EGFP and FLAG-APEX2-TFRC using Lipofectamine 2000 reagent. After transfection, ManII-EGFP was released from hook by giving biotin (40 μM) for 60 min. Cells were then incubated in EBSS or in full media (as indicated in the figures). Samples were then incubated with biotin-phenol (0.5mM) for 45 min followed by incubation with H$_2$O$_2$ for 1 min. Cells were washed three times with quenching buffer (Dulbecco's PBS supplemented with 10 mM sodium ascorbate, 10 mM sodium azide, and 5 mM trolox). Samples were lysed in RIPA lysis buffer. Protein concentrations of lysates were measured, and lysates were incubated with streptavidin beads (Thermo Fisher Scientific) overnight at 4°C. Samples were washed three time with lysis buffer. Proteins were eluted by boiling beads in 2× SDS sample buffer supplemented with 2 mM biotin. Eluted samples and corresponding lysates were subjected to SDS-PAGE followed by western blotting of target proteins.

High content microscopy—HCM was performed as described previously (Kumar et al., 2019). Briefly, cells were plated in 96 well plates and were transfected with plasmids whenever required (as indicated in figures). Cells were stimulated for autophagy by incubating in EBSS for 2h followed by fixation with 4% paraformaldehyde for 5 mins. Cells were permeabilized with 0.1% saponin and blocked in 3% BSA for 30 mins followed by incubation with primary antibody for 6 h and secondary antibody for 1 h. High content microscopy with automated image acquisition and quantification was carried out using a

Cellomics HCS scanner and iDEV software (Thermo) in 96-well plates (Kumar et al., 2019). For HCM experiments >500 primary objects were counted per well, minimum 6 wells were counted per experiments and data presented in figures are derived from at least 3 independent experiments.

Lipophagy-lipolysis assay—HeLaWT or E-SYT2KO cells were plated in 96 well plates. Cells were incubated with oleic acid (500μM) for 20h. Cells were then left in full media or incubated with EBSS for 16h. After completion of treatment times, cells were fixed in 4% PFA followed by two washings with PBS. Cells were then stained with BODIPY (1:500) (ThermoFisher) and Hoechst (1:000) for 15 min followed by three washes with PBS. Finally, lipid droplets were imaged and quantified using HCM as detailed above.

High content microscopy for Keima probes—293A WT or SIGMAR1[KO] cells were plated in 96 well plates and transfected with indicated Keima plasmids. Cells were incubated in full media or induced for autophagy by incubating with EBSS for 8h. Cells were then incubated in full media and incubated with Hoechst 33342 for ten minutes in full media and then acquired for Keima fluorescence at 440nm and 560 nm using the Cell Insight CX7 High-Content Screening (HCS) Platform (Thermo)(Kumar et al., 2019).

In vitro fusion ivitHC assay—In vitro fusion assay was developed for HCM platform by modifying a previously described assay (Matsui et al., 2018a; Moreau et al., 2011). For in vitro assay, cells were transfected with GFP-FIP200 and mCherry-ATG16L1, post-nuclear supernatants (PNS) were prepared by homogenizing cells in buffer containing 20 mM HEPES-KOH, pH 7.2, 400 mM sucrose, and 1 mM EDTA. Homogenate were centrifuged at 12000g for 15 min. PNS containing GFP-FIP200 and mCherry-ATG16L1 membranes were mixed for 60 min in the presence of an ATP regenerative system at 37°C. Control samples were left on ice. In experiments when BAPTA was added to the fusion reaction it was used at 20 μM. After the reaction, the samples were fixed with 2% paraformaldehyde in PBS for 15 min, centrifuged to remove the fixative (12,000g for 15 min), resuspended in mounting media and dispensed in 96 well plates (40 μl/well, at least 5 wells per sample). The plates were centrifuged at 500g for 1 min to allow settling down of the membranes to bottom of the plate. The plates were scanned in Cell Insight CX7 High-Content Screening (HCS) Platform (Thermo). A minimum of 10,000 objects were scanned per well and 5 wells per sample were used for analysis.

Super-resolution microscopy—Super-resolution imaging, and analysis were done as described previously (Kumar et al., 2019; Kumar et al., 2018). WT or STX17[KO] HeLa cells were plated on 25 mm coverslips (Warner instruments) and allowed to attach, cells were then transfected with FLAG-ATG16L1. After overnight transfection, cells were induced for autophagy by incubating with EBSS for 2h followed by fixation in 4% PFA for 5 min. After fixation, cells were incubated with anti-rabbit-FIP200 and anti-mouse FLAG antibodies for 4h and washed with PBS, followed by labeling with Alexa Fluor 647 (Invitrogen, A21245). The coverslip was mounted on an Attofluor cell chamber (A-7816, life technologies) with 1.1 ml of the imaging buffer. The imaging and center-to-center distances between FLAG-

ATG16L1 and FIP200 cluster centroids per ROI (region of interest) were calculated as described earlier (Kumar et al., 2018).

Immunofluorescence confocal microscopy—Immunofluorescence confocal microscopy was carried out as described previously (Kumar et al., 2019). Briefly, cells were plated onto coverslips in 6 well or 12-well plates. Cells were transfected with plasmids as indicated in Figures. Transfected cells were incubated in full media or EBSS (Earle's Balanced Salt Solution) for 2h and fixed in 4% paraformaldehyde for 10 min followed by permeabilization with 0.1% saponin in 3% BSA. Cells were blocked 3% BSA and then incubated with primary antibodies for 4h. Cells were washed three times with PBS and then incubated with appropriate secondary antibodies (Invitrogen) for 1 h at room temperature. Coverslips were then mounted using ProLong Gold Antifade Mountant (Invitrogen) and analyzed by confocal microscopy using the Zeiss LSM510 Laser Scanning Microscope.

Correlative Light-Electron Microscopy—For correlative light-electron microscopy (CLEM), the cells were grown on glass-bottom, gridded Mattek dishes (Cat No P35G-1.5–14-CGRD). Cells were induced for autophagy by incubation in EBSS, followed by fixation in 4% paraformaldehyde in 0.2 M Hepes, pH 7.4 for 10 min at room temperature, and imaged using phase contrast and confocal microscopy to record the cell positions and the fluorescent signals, respectively. The cells were then firmly fixed for electron microscopy using 2% glutaraldehyde in 0.2 M Hepes, pH 7.4, and stored in the same buffer at +4 C. For epon embedding, the cells were postfixed in osmium tetroxide, dehydrated in ethanol, and flat embedded in epon. The Matted grid was used to locate the cells of interest for thin sectioning. Serial 70-nm sections were cut, placed on single-slot girds and stained with uranyl acetate and lead citrate. Imaging was done with a Jeol JEM 1400 Plus transmission electron microscope. A high magnification TEM micrograph was aligned with a low magnification TEM micrograph, showing the whole cell. The fluorescent image was then correlated to the low magnification TEM micrograph based on the shape of the cell and nucleus as well as lipid droplets that are visible in both TEM and fluorescent images. The alignment and correlation was performed using TrakEM2 software version 1.3.6 (Cardona et al., 2012) as part of the Fiji distribution of ImageJ version 1.53i (Schindelin et al., 2012).

Membrane fractionation—Membrane fractionation was carried out as described previously(Kumar et al., 2019). Briefly, 293T cells (3 dishes per sample) were plated in 10 cm dishes, harvested, and homogenized by passing through a 22-G needle. Homogenates were subjected to sequential differential centrifugation at $3,000 \times g$ (10 min) and $25,000 \times g$ (20 min) to collect the pelleted membranes (TLA100.3 rotor, Beckman, polypropylene tube; Beckman). 25K membrane pellets were suspended in 1 ml 19% OptiPrep for a step gradient containing 0.5 ml 22.5%, 1 ml 19% (sample), 0.9 ml 16%, 0.9 ml 12%, 1 ml 8%, 0.5 ml 5% and 0.2 ml 0% OptiPrep each. The OptiPrep gradient was centrifuged at $150,000 \times g$ for 3 h and subsequently eight fractions, 0.5 ml each, were collected from the top. Fractions were diluted with B88 buffer (20 mM HEPES, pH 7.2, 150 mM potassium acetate, 5 mM magnesium acetate, 250 mM sorbitol) and membranes were collected by centrifugation at $100,000 \times g$ for 1 h. Sample were subjected to SDS-PAGE and western blot for FIP200, ATG16L1, GM130 and LC3 was done as described under immunoblotting.

Cholera Toxin B uptake assay—Cells were plated in 96 well plates and after suitable transfections (as indicated in figures), cells were incubated with Alexa Fluor-488-conjugated cholera toxin subunit B (ThermoFisher) for 15 min at 4°C (allowing toxin to bind to the plasma membrane). Then cells were incubated at 37°C (allowing internalization of cholera toxin) for 10 min and fixed for HCM analysis.

Protease protection assay—E-SYT2[KO] and wild type HeLa cells, and SIGMAR1[KO] and parental 293A cells were seeded into 10cm dishes and induced for autophagy by incubation in EBSS for 2h in presence of 100 nM bafilomycin A1. After treatment, cells were homogenized in buffer containing 20 mM HEPES-KOH, pH 7.2, 400 mM sucrose, and 1 mM EDTA. Cells were harvested and centrifuged at 500 g at 4°C, the postnuclear supernatant was collected and was equally divided into three parts, one of the samples was left untreated, and the other two were incubated with 25 μg/ml PK only in presence or absence of Triton X-100 (TX-100; 0.2%) for 10 min on ice. All samples were then subjected to TCA precipitation, and protein pellets were resuspended in the same volume of 2 x sample buffer. Approximately 40–60 μg of each sample was analyzed by immunoblotting.

SARS-CoV-2 infection—Cells were infected with the indicated MOI with SARS-CoV-2, isolate USA-WA/1/2020 (deposited by the Centers for Disease Control and Prevention and obtained through BEI Resources, NIAID, NIH, NR-52281). Cell death was measured at the indicated times using the CyQUANT XTT cell viability assay (ThermoFisher) according to the manufacturer's protocol. For HCM, Calu-3 and Huh7 cells were seeded in 96 well plates and transfected with FLAG-ATG16L1 and then taken to BSL3 facility. Half of the plate was incubated in EBSS (2h). Cells were then infected with SARS-CoV-2 (MOI:1) for 24h. Cells were then fixed with 4% paraformaldehyde for 15 min. Plates were decontaminated, permeabilized with 0.2% saponin and blocked with 3% BSA for 30 min and stained with FLAG and FIP200 antibodies. HCM was performed as detailed under HCM section.

APEX2-labeling and streptavidin enrichment for Mass Spectrometry—
HEK293T Flp-In-nsp6 [TetON] cells were left in full media or incubated with EBSS for 2h. Cells were then incubated in 500 μM biotin-phenol for the last 30 min of EBSS incubation. Cells were then incubated in 1 mM H_2O_2 at room temperature. The reaction was stopped with quenching buffer (10 mM sodium ascorbate, 10 mM sodium azide and 5 mM Trolox in Dulbecco's Phosphate Buffered Saline [DPBS]). All samples were washed three times with quenching buffer, and twice with DPBS. For LC-MS/MS analysis, cell pellets were lysed in 500 μL ice-cold lysis buffer (6 M urea, 0.3 M NaCl, 1 mM EDTA, 1 mM EGTA, 10 mM sodium ascorbate, 10 mM sodium azide, 5 mM Trolox, 1% glycerol and 25 mm Tris/HCl [PH 7.5]) for 30 min by gentle pipetting. Lysates were clarified by centrifugation and protein concentrations were quantified. Streptavidin-coated magnetic beads (Pierce) were washed with lysis buffer. 3 mg of each sample was mixed with 100 μL of streptavidin bead. The suspensions were gently rotated at 4°C overnight to bind biotinylated proteins. The flowthrough after enrichment was removed and the beads were washed in sequence with 1 mL IP buffer (150 mM NaCl, 10 mM Tris-HCl [pH 8.0], 1 mM EDTA, 1 mM EGTA, 1% Triton X-100) twice; 1 mL 1M KCl; 1 mL of 50 mM Na_2CO_3; 1 mL 2 M Urea in 20 mM

Tris HCl (pH 8); 1 mL IP buffer. Biotinylated proteins were eluted and processed for mass spectrometry.

LC-MS/MS (Sample preparation)—Protein samples on magnetic beads were washed four times with 200ul of 50mM Triethyl ammonium bicarbonate (TEAB) with a twenty-minute shake time at 4°C in between each wash. Roughly 2.5 μg of trypsin was added to the bead and TEAB mixture and the samples were digested overnight at 800 rpm shake speed. After overnight digestion the supernatant was removed, and the beads were washed once with 50mM ammonium bicarbonate. After 20 minutes at a gentle shake the wash is removed and combined with the initial supernatant. The peptide extracts were reduced in volume by vacuum centrifugation and a small portion of the extract was used for fluorometric peptide quantification (Thermo scientific Pierce). One microgram of sample based on the fluorometric peptide assay was loaded for each LC-MS analysis.

Liquid Chromatography Tandem Mass Spectrometry—Peptides were analyzed by LC-MS/MS by trapping on a C18 peptide trapping column (Thermo Scientific) and separated on a Pepsep 8 cm × 150 um C18 column (Merslev, Denmark) using a Dionex Ultimate 3000 nUPLC. Samples were run on Thermo Scientific Exploris 480 mass spectrometer for 90 min using Data independent Acquisition mode (DIA). DIA was acquired between 360–1200 Da with 45 Da non-overlapping windows. MS1 resolution was set at 120K and MS2 at 30K, MS1 normalized AGC target of 300% and MS2 1000% respectively.

Data Analysis—DIA data was analyzed using Spectronaut 15 with directDIA workflow and default settings.

Flow cytometry to analyze intracellular calcium—Intracellular calcium was analyzed using FLUO-3AM fluorescence on the FL-1 channel of flow cytometer (BD FACScan). Wild type HeLa or STX17Ko cells were left unstimulated on incubated in HBSS for 2h. Cells were incubated with 5μM of FLUO-3AM for 30 minutes, followed by analysis on flow cytometer.

Immunoblotting and co-immunoprecipitation assays—Immunoblotting and co-immunoprecipitation (co-IP) were performed as described previously(Kumar et al., 2018). For co-IP, cells were transfected with 10 μg of plasmids, wherever stated, and lysed in NP-40 buffer containing protease inhibitor cocktail (Roche, cat# 11697498001) and PMSF (Sigma, cat# 93482). Lysates were mixed with 5 μg antibody and incubated at 4°C for overnight followed by incubation with Dynabeads protein G (Life Technologies) for 4 h, at 4°C. Beads were washed three times with PBS and then boiled with SDS-PAGE buffer for analysis of interacting protein by immunoblotting.

Quantification and statistical analysis

Data are expressed as means ± SEM (n ≥ 3). Data were analyzed with a paired two-tailed Student's *t*-test or analysis of variance (ANOVA). Statistical significance was defined as † p ≥ 0.05, *$P < 0.05$, **p<0.01.

Supplementary Material

Refer to Web version on PubMed Central for supplementary material.

Acknowledgments

References

Alsaadi RM, Losier TT, Tian W, Jackson A, Guo Z, Rubinsztein DC, and Russell RC (2019). ULK1-mediated phosphorylation of ATG16L1 promotes xenophagy, but destabilizes the ATG16L1 Crohn's mutant. EMBO Rep 20, e46885. [PubMed: 31267703]

An H, and Harper JW (2018). Systematic analysis of ribophagy in human cells reveals bystander flux during selective autophagy. Nat Cell Biol 20, 135–143. [PubMed: 29230017]

An H, Ordureau A, Korner M, Paulo JA, and Harper JW (2020). Systematic quantitative analysis of ribosome inventory during nutrient stress. Nature 583, 303–309. [PubMed: 32612236]

Angelini MM, Akhlaghpour M, Neuman BW, and Buchmeier MJ (2013). Severe acute respiratory syndrome coronavirus nonstructural proteins 3, 4, and 6 induce double-membrane vesicles. mBio 4.

Arasaki K, Nagashima H, Kurosawa Y, Kimura H, Nishida N, Dohmae N, Yamamoto A, Yanagi S, Wakana Y, Inoue H, et al. (2018). MAP1B-LC1 prevents autophagosome formation by linking syntaxin 17 to microtubules. EMBO Rep.

Axe EL, Walker SA, Manifava M, Chandra P, Roderick HL, Habermann A, Griffiths G, and Ktistakis NT (2008). Autophagosome formation from membrane compartments enriched in phosphatidylinositol 3-phosphate and dynamically connected to the endoplasmic reticulum. J Cell Biol 182, 685–701. [PubMed: 18725538]

Bakula D, Muller AJ, Zuleger T, Takacs Z, Franz-Wachtel M, Thost AK, Brigger D, Tschan MP, Frickey T, Robenek H, et al. (2017). WIPI3 and WIPI4 beta-propellers are scaffolds for LKB1-AMPK-TSC signalling circuits in the control of autophagy. Nat Commun 8, 15637. [PubMed: 28561066]

Bas L, Papinski D, Licheva M, Torggler R, Rohringer S, Schuschnig M, and Kraft C (2018). Reconstitution reveals Ykt6 as the autophagosomal SNARE in autophagosome-vacuole fusion. J Cell Biol.

Baskaran S, Carlson LA, Stjepanovic G, Young LN, Kim do J., Grob P, Stanley RE, Nogales E, and Hurley JH (2014). Architecture and dynamics of the autophagic phosphatidylinositol 3-kinase complex. Elife 3.

Bissa B, and Deretic V (2018). Autophagosome Formation: Cutting the Gordian Knot at the ER. Curr Biol 28, R347–R349. [PubMed: 29689207]

Bjorkoy G, Lamark T, Brech A, Outzen H, Perander M, Overvatn A, Stenmark H, and Johansen T (2005). p62/SQSTM1 forms protein aggregates degraded by autophagy and has a protective effect on huntingtin-induced cell death. J Cell Biol 171, 603–614. [PubMed: 16286508]

Boncompain G, Divoux S, Gareil N, de Forges H, Lescure A, Latreche L, Mercanti V, Jollivet F, Raposo G, and Perez F (2012). Synchronization of secretory protein traffic in populations of cells. Nat Methods 9, 493–498. [PubMed: 22406856]

Bradfute SB, Hurwitz I, Yingling AV, Ye C, Cheng Q, Noonan TP, Raval JS, Sosa NR, Mertz GJ, Perkins DJ, et al. (2020). Severe Acute Respiratory Syndrome Coronavirus 2 Neutralizing Antibody Titers in Convalescent Plasma and Recipients in New Mexico: An Open Treatment Study in Patients With Coronavirus Disease 2019. J Infect Dis 222, 1620–1628. [PubMed: 32779705]

Brewer KD, Bacaj T, Cavalli A, Camilloni C, Swarbrick JD, Liu J, Zhou A, Zhou P, Barlow N, Xu J, et al. (2015). Dynamic binding mode of a Synaptotagmin-1-SNARE complex in solution. Nat Struct Mol Biol 22, 555–564. [PubMed: 26030874]

Brose N, Petrenko AG, Sudhof TC, and Jahn R (1992). Synaptotagmin: a calcium sensor on the synaptic vesicle surface. Science 256, 1021–1025. [PubMed: 1589771]

Cardenas C, Miller RA, Smith I, Bui T, Molgo J, Muller M, Vais H, Cheung KH, Yang J, Parker I, et al. (2010). Essential regulation of cell bioenergetics by constitutive InsP3 receptor Ca2+ transfer to mitochondria. Cell 142, 270–283. [PubMed: 20655468]

Cardona A, Saalfeld S, Schindelin J, Arganda-Carreras I, Preibisch S, Longair M, Tomancak P, Hartenstein V, and Douglas RJ (2012). TrakEM2 software for neural circuit reconstruction. PLoS One 7, e38011. [PubMed: 22723842]

Chang C, Young LN, Morris KL, von Bulow S., Schoneberg J, Yamamoto-Imoto H, Oe Y, Yamamoto K, Nakamura S, Stjepanovic G, et al. (2019). Bidirectional Control of Autophagy by BECN1 BARA Domain Dynamics. Mol Cell 73, 339–353 e336. [PubMed: 30581147]

Chapman ER (2002). Synaptotagmin: a Ca(2+) sensor that triggers exocytosis? Nat Rev Mol Cell Biol 3, 498–508. [PubMed: 12094216]

Chauhan S, Kumar S, Jain A, Ponpuak M, Mudd MH, Kimura T, Choi SW, Peters R, Mandell M, Bruun JA, et al. (2016). TRIMs and Galectins Globally Cooperate and TRIM16 and Galectin-3 Co-direct Autophagy in Endomembrane Damage Homeostasis. Dev Cell 39, 13–27. [PubMed: 27693506]

Chauhan S, Mandell MA, and Deretic V (2015). IRGM Governs the Core Autophagy Machinery to Conduct Antimicrobial Defense. Mol Cell 58, 507–521. [PubMed: 25891078]

Christ MG, Huesmann H, Nagel H, Kern A, and Behl C (2019). Sigma-1 Receptor Activation Induces Autophagy and Increases Proteostasis Capacity In Vitro and In Vivo. Cells 8.

Cottam EM, Maier HJ, Manifava M, Vaux LC, Chandra-Schoenfelder P, Gerner W, Britton P, Ktistakis NT, and Wileman T (2011). Coronavirus nsp6 proteins generate autophagosomes from the endoplasmic reticulum via an omegasome intermediate. Autophagy 7, 1335–1347. [PubMed: 21799305]

Cottam EM, Whelband MC, and Wileman T (2014). Coronavirus NSP6 restricts autophagosome expansion. Autophagy 10, 1426–1441. [PubMed: 24991833]

Criollo A, Maiuri MC, Tasdemir E, Vitale I, Fiebig AA, Andrews D, Molgo J, Diaz J, Lavandero S, Harper F, et al. (2007). Regulation of autophagy by the inositol trisphosphate receptor. Cell Death Differ 14, 1029–1039. [PubMed: 17256008]

Deretic V (2021). Autophagy in inflammation, infection, and immunometabolism. Immunity 54, 437–453. [PubMed: 33691134]

Deretic V, and Kroemer G (2021). Autophagy in metabolism and quality control: opposing, complementary or interlinked functions? Autophagy, 1–10.

Diao J, Liu R, Rong Y, Zhao M, Zhang J, Lai Y, Zhou Q, Wilz LM, Li J, Vivona S, et al. (2015). ATG14 promotes membrane tethering and fusion of autophagosomes to endolysosomes. Nature 520, 563–566. [PubMed: 25686604]

Dooley HC, Razi M, Polson HE, Girardin SE, Wilson MI, and Tooze SA (2014). WIPI2 Links LC3 Conjugation with PI3P, Autophagosome Formation, and Pathogen Clearance by Recruiting Atg12–5-16L1. Mol Cell 55, 238–252. [PubMed: 24954904]

EA JA, and Jones IM (2019). Membrane binding proteins of coronaviruses. Future Virol 14, 275–286. [PubMed: 32201500]

Egan DF, Shackelford DB, Mihaylova MM, Gelino S, Kohnz RA, Mair W, Vasquez DS, Joshi A, Gwinn DM, Taylor R, et al. (2011). Phosphorylation of ULK1 (hATG1) by AMP-activated protein kinase connects energy sensing to mitophagy. Science 331, 456–461. [PubMed: 21205641]

Engedal N, Torgersen ML, Guldvik IJ, Barfeld SJ, Bakula D, Saetre F, Hagen LK, Patterson JB, Proikas-Cezanne T, Seglen PO, et al. (2013). Modulation of intracellular calcium homeostasis blocks autophagosome formation. Autophagy 9, 1475–1490. [PubMed: 23970164]

Eskelinen EL (2008). Fine structure of the autophagosome. Methods Mol Biol 445, 11–28. [PubMed: 18425441]

Feher A, Juhasz A, Laszlo A, Kalman J Jr., Pakaski M, Kalman J, and Janka Z (2012). Association between a variant of the sigma-1 receptor gene and Alzheimer's disease. Neurosci Lett 517, 136–139. [PubMed: 22561649]

Fletcher K, Ulferts R, Jacquin E, Veith T, Gammoh N, Arasteh JM, Mayer U, Carding SR, Wileman T, Beale R, et al. (2018). The WD40 domain of ATG16L1 is required for its non-canonical role in lipidation of LC3 at single membranes. EMBO J 37.

Fujita N, Morita E, Itoh T, Tanaka A, Nakaoka M, Osada Y, Umemoto T, Saitoh T, Nakatogawa H, Kobayashi S, et al. (2013). Recruitment of the autophagic machinery to endosomes during infection is mediated by ubiquitin. J Cell Biol 203, 115–128. [PubMed: 24100292]

Fung TS, and Liu DX (2019). Human Coronavirus: Host-Pathogen Interaction. Annu Rev Microbiol 73, 529–557. [PubMed: 31226023]

Galluzzi L, and Green DR (2019). Autophagy-Independent Functions of the Autophagy Machinery. Cell 177, 1682–1699. [PubMed: 31199916]

Gammoh N, Florey O, Overholtzer M, and Jiang X (2013). Interaction between FIP200 and ATG16L1 distinguishes ULK1 complex-dependent and -independent autophagy. Nat Struct Mol Biol 20, 144–149. [PubMed: 23262492]

Ganley IG, Lam du H., Wang J, Ding X, Chen S, and Jiang X (2009). ULK1.ATG13.FIP200 complex mediates mTOR signaling and is essential for autophagy. J Biol Chem 284, 12297–12305. [PubMed: 19258318]

Ganley IG, Wong PM, Gammoh N, and Jiang X (2011). Distinct autophagosomal-lysosomal fusion mechanism revealed by thapsigargin-induced autophagy arrest. Mol Cell 42, 731–743. [PubMed: 21700220]

Gao J, Reggiori F, and Ungermann C (2018). A novel in vitro assay reveals SNARE topology and the role of Ykt6 in autophagosome fusion with vacuoles. J Cell Biol.

Gassen NC, Niemeyer D, Muth D, Corman VM, Martinelli S, Gassen A, Hafner K, Papies J, Mosbauer K, Zellner A, et al. (2019). SKP2 attenuates autophagy through Beclin1-ubiquitination and its inhibition reduces MERS-Coronavirus infection. Nature communications 10, 5770.

Ge L, Melville D, Zhang M, and Schekman R (2013). The ER-Golgi intermediate compartment is a key membrane source for the LC3 lipidation step of autophagosome biogenesis. Elife 2, e00947. [PubMed: 23930225]

Ge L, Zhang M, Kenny SJ, Liu D, Maeda M, Saito K, Mathur A, Xu K, and Schekman R (2017). Remodeling of ER-exit sites initiates a membrane supply pathway for autophagosome biogenesis. EMBO Rep 18, 1586–1603. [PubMed: 28754694]

Ge L, Zhang M, and Schekman R (2014). Phosphatidylinositol 3-kinase and COPII generate LC3 lipidation vesicles from the ER-Golgi intermediate compartment. Elife 3, e04135. [PubMed: 25432021]

Ghosh S, Dellibovi-Ragheb TA, Kerviel A, Pak E, Qiu Q, Fisher M, Takvorian PM, Bleck C, Hsu VW, Fehr AR, et al. (2020). beta-Coronaviruses Use Lysosomes for Egress Instead of the Biosynthetic Secretory Pathway. Cell.

Giordano F, Saheki Y, Idevall-Hagren O, Colombo SF, Pirruccello M, Milosevic I, Gracheva EO, Bagriantsev SN, Borgese N, and De Camilli P (2013). PI(4,5)P(2)-dependent and Ca(2+)-regulated ER-PM interactions mediated by the extended synaptotagmins. Cell 153, 1494–1509. [PubMed: 23791178]

Gordon DE, Jang GM, Bouhaddou M, Xu J, Obernier K, White KM, O'Meara MJ, Rezelj VV, Guo JZ, Swaney DL, et al. (2020). A SARS-CoV-2 protein interaction map reveals targets for drug repurposing. Nature.

Gu Y, Princely Abudu Y., Kumar S, Bissa B, Choi SW, Jia J, Lazarou M, Eskelinen EL, Johansen T, and Deretic V (2019). Mammalian Atg8 proteins regulate lysosome and autolysosome biogenesis through SNAREs. EMBO J 38, e101994. [PubMed: 31625181]

Guo B, Liang Q, Li L, Hu Z, Wu F, Zhang P, Ma Y, Zhao B, Kovacs AL, Zhang Z, et al. (2014). O-GlcNAc-modification of SNAP-29 regulates autophagosome maturation. Nat Cell Biol 16, 1215–1226. [PubMed: 25419848]

Guo L, Yu H, Gu W, Luo X, Li R, Zhang J, Xu Y, Yang L, Shen N, Feng L, et al. (2016). Autophagy Negatively Regulates Transmissible Gastroenteritis Virus Replication. Sci Rep 6, 23864. [PubMed: 27029407]

Guo X, Zhang M, Zhang X, Tan X, Guo H, Zeng W, Yan G, Memon AM, Li Z, Zhu Y, et al. (2017). Porcine Epidemic Diarrhea Virus Induces Autophagy to Benefit Its Replication. Viruses 9.

Hailey DW, Rambold AS, Satpute-Krishnan P, Mitra K, Sougrat R, Kim PK, and Lippincott-Schwartz J (2010). Mitochondria supply membranes for autophagosome biogenesis during starvation. Cell 141, 656–667. [PubMed: 20478256]

Hamasaki M, Furuta N, Matsuda A, Nezu A, Yamamoto A, Fujita N, Oomori H, Noda T, Haraguchi T, Hiraoka Y, et al. (2013). Autophagosomes form at ER-mitochondria contact sites. Nature 495, 389–393. [PubMed: 23455425]

Hara T, Takamura A, Kishi C, Iemura S, Natsume T, Guan JL, and Mizushima N (2008). FIP200, a ULK-interacting protein, is required for autophagosome formation in mammalian cells. J Cell Biol 181, 497–510. [PubMed: 18443221]

Hayashi T, and Su TP (2007). Sigma-1 receptor chaperones at the ER-mitochondrion interface regulate Ca(2+) signaling and cell survival. Cell 131, 596–610. [PubMed: 17981125]

Hayashi-Nishino M, Fujita N, Noda T, Yamaguchi A, Yoshimori T, and Yamamoto A (2009). A subdomain of the endoplasmic reticulum forms a cradle for autophagosome formation. Nat Cell Biol 11, 1433–1437. [PubMed: 19898463]

Heckmann BL, Teubner BJW, Tummers B, Boada-Romero E, Harris L, Yang M, Guy CS, Zakharenko SS, and Green DR (2019). LC3-Associated Endocytosis Facilitates beta-Amyloid Clearance and Mitigates Neurodegeneration in Murine Alzheimer's Disease. Cell 178, 536–551 e514. [PubMed: 31257024]

Hirata Y, Yamamoto H, Atta MS, Mahmoud S, Oh-hashi K, and Kiuchi K (2011). Chloroquine inhibits glutamate-induced death of a neuronal cell line by reducing reactive oxygen species through sigma-1 receptor. J Neurochem 119, 839–847. [PubMed: 21883227]

Hoffmann HH, Schneider WM, Rozen-Gagnon K, Miles LA, Schuster F, Razooky B, Jacobson E, Wu X, Yi S, Rudin CM, et al. (2021). TMEM41B Is a Pan-flavivirus Host Factor. Cell 184, 133–148 e120. [PubMed: 33338421]

Hoffmann M, Kleine-Weber H, Schroeder S, Kruger N, Herrler T, Erichsen S, Schiergens TS, Herrler G, Wu NH, Nitsche A, et al. (2020a). SARS-CoV-2 Cell Entry Depends on ACE2 and TMPRSS2 and Is Blocked by a Clinically Proven Protease Inhibitor. Cell 181, 271–280 e278. [PubMed: 32142651]

Hoffmann M, Mosbauer K, Hofmann-Winkler H, Kaul A, Kleine-Weber H, Kruger N, Gassen NC, Muller MA, Drosten C, and Pohlmann S (2020b). Chloroquine does not inhibit infection of human lung cells with SARS-CoV-2. Nature.

Hosokawa N, Hara T, Kaizuka T, Kishi C, Takamura A, Miura Y, Iemura S, Natsume T, Takehana K, Yamada N, et al. (2009). Nutrient-dependent mTORC1 association with the ULK1-Atg13-FIP200 complex required for autophagy. Mol Biol Cell 20, 1981–1991. [PubMed: 19211835]

Inoki K, Kim J, and Guan KL (2012). AMPK and mTOR in cellular energy homeostasis and drug targets. Annu Rev Pharmacol Toxicol 52, 381–400. [PubMed: 22017684]

Itakura E, Kishi-Itakura C, and Mizushima N (2012). The hairpin-type tail-anchored SNARE syntaxin 17 targets to autophagosomes for fusion with endosomes/lysosomes. Cell 151, 1256–1269. [PubMed: 23217709]

Itakura E, and Mizushima N (2010). Characterization of autophagosome formation site by a hierarchical analysis of mammalian Atg proteins. Autophagy 6.

Itakura E, and Mizushima N (2011). p62 Targeting to the autophagosome formation site requires self-oligomerization but not LC3 binding. The Journal of cell biology 192, 17–27. [PubMed: 21220506]

Jacquin E, Leclerc-Mercier S, Judon C, Blanchard E, Fraitag S, and Florey O (2017). Pharmacological modulators of autophagy activate a parallel noncanonical pathway driving unconventional LC3 lipidation. Autophagy 13, 854–867. [PubMed: 28296541]

Jung CH, Jun CB, Ro SH, Kim YM, Otto NM, Cao J, Kundu M, and Kim DH (2009). ULK-Atg13-FIP200 complexes mediate mTOR signaling to the autophagy machinery. Mol Biol Cell 20, 1992–2003. [PubMed: 19225151]

Katayama H, Kogure T, Mizushima N, Yoshimori T, and Miyawaki A (2011). A sensitive and quantitative technique for detecting autophagic events based on lysosomal delivery. Chem Biol 18, 1042–1052. [PubMed: 21867919]

Kim J, Kundu M, Viollet B, and Guan KL (2011). AMPK and mTOR regulate autophagy through direct phosphorylation of Ulk1. Nat Cell Biol 13, 132–141. [PubMed: 21258367]

Klionsky DJ, Abdelmohsen K, Abe A, Abedin MJ, Abeliovich H, Acevedo Arozena A, Adachi H, Adams CM, Adams PD, Adeli K, et al. (2016). Guidelines for the use and interpretation of assays for monitoring autophagy (3rd edition). Autophagy 12, 1–222. [PubMed: 26799652]

Klionsky DJ, Petroni G, Amaravadi RK, Baehrecke EH, Ballabio A, Boya P, Bravo-San Pedro J.M., Cadwell K, Cecconi F, Choi AMK, et al. (2021). Autophagy in major human diseases. EMBO J, e108863. [PubMed: 34459017]

Knaevelsrud H, Soreng K, Raiborg C, Haberg K, Rasmuson F, Brech A, Liestol K, Rusten TE, Stenmark H, Neufeld TP, et al. (2013). Membrane remodeling by the PX-BAR protein SNX18 promotes autophagosome formation. J Cell Biol 202, 331–349. [PubMed: 23878278]

Knoops K, Kikkert M, Worm SH, Zevenhoven-Dobbe JC, van der Meer Y, Koster AJ, Mommaas AM, and Snijder EJ (2008). SARS-coronavirus replication is supported by a reticulovesicular network of modified endoplasmic reticulum. PLoS Biol 6, e226. [PubMed: 18798692]

Ko S, Gu MJ, Kim CG, Kye YC, Lim Y, Lee JE, Park BC, Chu H, Han SH, and Yun CH (2017). Rapamycin-induced autophagy restricts porcine epidemic diarrhea virus infectivity in porcine intestinal epithelial cells. Antiviral Res 146, 86–95. [PubMed: 28842266]

Kopitz J, Kisen GO, Gordon PB, Bohley P, and Seglen PO (1990). Nonselective autophagy of cytosolic enzymes by isolated rat hepatocytes. J Cell Biol 111, 941–953. [PubMed: 2391370]

Kumar S, Gu Y, Abudu YP, Bruun JA, Jain A, Farzam F, Mudd M, Anonsen JH, Rusten TE, Kasof G, et al. (2019). Phosphorylation of Syntaxin 17 by TBK1 Controls Autophagy Initiation. Dev Cell.

Kumar S, Jain A, Choi SW, da Silva GPD, Allers L, Mudd MH, Peters RS, Anonsen JH, Rusten TE, Lazarou M, et al. (2020). Mammalian Atg8 proteins and the autophagy factor IRGM control mTOR and TFEB at a regulatory node critical for responses to pathogens. Nat Cell Biol 22, 973–985. [PubMed: 32753672]

Kumar S, Jain A, Farzam F, Jia J, Gu Y, Choi SW, Mudd MH, Claude-Taupin A, Wester MJ, Lidke KA, et al. (2018). Mechanism of Stx17 recruitment to autophagosomes via IRGM and mammalian Atg8 proteins. J Cell Biol 217, 997–1013. [PubMed: 29420192]

Lamb CA, Yoshimori T, and Tooze SA (2013). The autophagosome: origins unknown, biogenesis complex. Nat Rev Mol Cell Biol 14, 759–774. [PubMed: 24201109]

Lazarou M, Sliter DA, Kane LA, Sarraf SA, Wang C, Burman JL, Sideris DP, Fogel AI, and Youle RJ (2015). The ubiquitin kinase PINK1 recruits autophagy receptors to induce mitophagy. Nature 524, 309–314. [PubMed: 26266977]

Levine B, and Kroemer G (2019). Biological Functions of Autophagy Genes: A Disease Perspective. Cell 176, 11–42. [PubMed: 30633901]

Longatti A, Lamb CA, Razi M, Yoshimura S, Barr FA, and Tooze SA (2012). TBC1D14 regulates autophagosome formation via Rab11- and ULK1-positive recycling endosomes. J Cell Biol 197, 659–675. [PubMed: 22613832]

Lystad AH, Carlsson SR, de la Ballina LR, Kauffman KJ, Nag S, Yoshimori T, Melia TJ, and Simonsen A (2019). Distinct functions of ATG16L1 isoforms in membrane binding and LC3B lipidation in autophagy-related processes. Nat Cell Biol 21, 372–383. [PubMed: 30778222]

MacLennan DH, and Kranias EG (2003). Phospholamban: a crucial regulator of cardiac contractility. Nat Rev Mol Cell Biol 4, 566–577. [PubMed: 12838339]

Maher CM, Thomas JD, Haas DA, Longen CG, Oyer HM, Tong JY, and Kim FJ (2018). Small-Molecule Sigma1 Modulator Induces Autophagic Degradation of PD-L1. Mol Cancer Res 16, 243–255. [PubMed: 29117944]

Martinez J, Malireddi RK, Lu Q, Cunha LD, Pelletier S, Gingras S, Orchard R, Guan JL, Tan H, Peng J, et al. (2015). Molecular characterization of LC3-associated phagocytosis reveals distinct roles for Rubicon, NOX2 and autophagy proteins. Nat Cell Biol 17, 893–906. [PubMed: 26098576]

Matsui T, Jiang P, Nakano S, Sakamaki Y, Yamamoto H, and Mizushima N (2018a). Autophagosomal YKT6 is required for fusion with lysosomes independently of syntaxin 17. J Cell Biol.

Matsui T, Jiang P, Nakano S, Sakamaki Y, Yamamoto H, and Mizushima N (2018b). Autophagosomal YKT6 is required for fusion with lysosomes independently of syntaxin 17. J Cell Biol 217, 2633–2645. [PubMed: 29789439]

Mauthe M, Orhon I, Rocchi C, Zhou X, Luhr M, Hijlkema KJ, Coppes RP, Engedal N, Mari M, and Reggiori F (2018). Chloroquine inhibits autophagic flux by decreasing autophagosome-lysosome fusion. Autophagy 14, 1435–1455. [PubMed: 29940786]

Mauvezin C, Nagy P, Juhasz G, and Neufeld TP (2015). Autophagosome-lysosome fusion is independent of V-ATPase-mediated acidification. Nat Commun 6, 7007. [PubMed: 25959678]

Melia TJ, Lystad AH, and Simonsen A (2020). Autophagosome biogenesis: From membrane growth to closure. J Cell Biol 219.

Miao G, Zhao H, Li Y, Ji M, Chen Y, Shi Y, Bi Y, Wang P, and Zhang H (2021). ORF3a of the COVID-19 virus SARS-CoV-2 blocks HOPS complex-mediated assembly of the SNARE complex required for autolysosome formation. Dev Cell 56, 427–442 e425. [PubMed: 33422265]

Min SW, Chang WP, and Sudhof TC (2007). E-Syts, a family of membranous Ca2+-sensor proteins with multiple C2 domains. Proc Natl Acad Sci U S A 104, 3823–3828. [PubMed: 17360437]

Mizushima N, Yoshimori T, and Ohsumi Y (2011). The role of Atg proteins in autophagosome formation. Annu Rev Cell Dev Biol 27, 107–132. [PubMed: 21801009]

Moreau K, Ravikumar B, Renna M, Puri C, and Rubinsztein DC (2011). Autophagosome precursor maturation requires homotypic fusion. Cell 146, 303–317. [PubMed: 21784250]

Morishita H, and Mizushima N (2019). Diverse Cellular Roles of Autophagy. Annu Rev Cell Dev Biol 35, 453–475. [PubMed: 31283377]

Narendra D, Tanaka A, Suen DF, and Youle RJ (2008). Parkin is recruited selectively to impaired mitochondria and promotes their autophagy. J Cell Biol 183, 795–803. [PubMed: 19029340]

Nascimbeni AC, Giordano F, Dupont N, Grasso D, Vaccaro MI, Codogno P, and Morel E (2017). ER-plasma membrane contact sites contribute to autophagosome biogenesis by regulation of local PI3P synthesis. EMBO J 36, 2018–2033. [PubMed: 28550152]

Nguyen TN, Padman BS, Usher J, Oorschot V, Ramm G, and Lazarou M (2016). Atg8 family LC3/GABARAP proteins are crucial for autophagosome-lysosome fusion but not autophagosome formation during PINK1/Parkin mitophagy and starvation. J Cell Biol 215, 857–874. [PubMed: 27864321]

Nishida Y, Arakawa S, Fujitani K, Yamaguchi H, Mizuta T, Kanaseki T, Komatsu M, Otsu K, Tsujimoto Y, and Shimizu S (2009). Discovery of Atg5/Atg7-independent alternative macroautophagy. Nature 461, 654–658. [PubMed: 19794493]

Nishimura T, Kaizuka T, Cadwell K, Sahani MH, Saitoh T, Akira S, Virgin HW, and Mizushima N (2013). FIP200 regulates targeting of Atg16L1 to the isolation membrane. EMBO Rep 14, 284–291. [PubMed: 23392225]

Nishimura T, Tamura N, Kono N, Shimanaka Y, Arai H, Yamamoto H, and Mizushima N (2017). Autophagosome formation is initiated at phosphatidylinositol synthase-enriched ER subdomains. EMBO J 36, 1719–1735. [PubMed: 28495679]

Pankiv S, Clausen TH, Lamark T, Brech A, Bruun JA, Outzen H, Overvatn A, Bjorkoy G, and Johansen T (2007). p62/SQSTM1 binds directly to Atg8/LC3 to facilitate degradation of ubiquitinated protein aggregates by autophagy. J Biol Chem 282, 24131–24145. [PubMed: 17580304]

Pattingre S, Bauvy C, and Codogno P (2003). Amino acids interfere with the ERK1/2-dependent control of macroautophagy by controlling the activation of Raf-1 in human colon cancer HT-29 cells. J Biol Chem 278, 16667–16674. [PubMed: 12609989]

Periasamy M, and Kalyanasundaram A (2007). SERCA pump isoforms: their role in calcium transport and disease. Muscle Nerve 35, 430–442. [PubMed: 17286271]

Pilli M, Arko-Mensah J, Ponpuak M, Roberts E, Master S, Mandell MA, Dupont N, Ornatowski W, Jiang S, Bradfute SB, et al. (2012). TBK-1 Promotes Autophagy-Mediated Antimicrobial Defense by Controlling Autophagosome Maturation. Immunity 37, 223–234. [PubMed: 22921120]

Prentice E, Jerome WG, Yoshimori T, Mizushima N, and Denison MR (2004). Coronavirus replication complex formation utilizes components of cellular autophagy. J Biol Chem 279, 10136–10141. [PubMed: 14699140]

Puri C, Renna M, Bento CF, Moreau K, and Rubinsztein DC (2013). Diverse autophagosome membrane sources coalesce in recycling endosomes. Cell 154, 1285–1299. [PubMed: 24034251]

Puri C, Vicinanza M, Ashkenazi A, Gratian MJ, Zhang Q, Bento CF, Renna M, Menzies FM, and Rubinsztein DC (2018). The RAB11A-Positive Compartment Is a Primary Platform for Autophagosome Assembly Mediated by WIPI2 Recognition of PI3P-RAB11A. Dev Cell 45, 114–131 e118. [PubMed: 29634932]

Ravenhill BJ, Boyle KB, von Muhlinen N, Ellison CJ, Masson GR, Otten EG, Foeglein A, Williams R, and Randow F (2019). The Cargo Receptor NDP52 Initiates Selective Autophagy by Recruiting the ULK Complex to Cytosol-Invading Bacteria. Mol Cell 74, 320–329 e326. [PubMed: 30853402]

Ravikumar B, Moreau K, Jahreiss L, Puri C, and Rubinsztein DC (2010). Plasma membrane contributes to the formation of pre-autophagosomal structures. Nat Cell Biol 12, 747–757. [PubMed: 20639872]

Reggiori F, Monastyrska I, Verheije MH, Cali T, Ulasli M, Bianchi S, Bernasconi R, de Haan CA, and Molinari M (2010). Coronaviruses Hijack the LC3-I-positive EDEMosomes, ER-derived vesicles exporting short-lived ERAD regulators, for replication. Cell Host Microbe 7, 500–508. [PubMed: 20542253]

Reggiori F, and Ungermann C (2017). Autophagosome Maturation and Fusion. J Mol Biol 429, 486–496. [PubMed: 28077293]

Saheki Y, Bian X, Schauder CM, Sawaki Y, Surma MA, Klose C, Pincet F, Reinisch KM, and De Camilli P (2016). Control of plasma membrane lipid homeostasis by the extended synaptotagmins. Nat Cell Biol 18, 504–515. [PubMed: 27065097]

Saitoh T, Fujita N, Jang MH, Uematsu S, Yang BG, Satoh T, Omori H, Noda T, Yamamoto N, Komatsu M, et al. (2008). Loss of the autophagy protein Atg16L1 enhances endotoxin-induced IL-1beta production. Nature 456, 264–268. [PubMed: 18849965]

Sanjuan MA, Dillon CP, Tait SW, Moshiach S, Dorsey F, Connell S, Komatsu M, Tanaka K, Cleveland JL, Withoff S, et al. (2007). Toll-like receptor signalling in macrophages links the autophagy pathway to phagocytosis. Nature 450, 1253–1257. [PubMed: 18097414]

Schindelin J, Arganda-Carreras I, Frise E, Kaynig V, Longair M, Pietzsch T, Preibisch S, Rueden C, Saalfeld S, Schmid B, et al. (2012). Fiji: an open-source platform for biological-image analysis. Nat Methods 9, 676–682. [PubMed: 22743772]

Schmidt HR, Zheng S, Gurpinar E, Koehl A, Manglik A, and Kruse AC (2016). Crystal structure of the human sigma1 receptor. Nature 532, 527–530. [PubMed: 27042935]

Schneider M, Ackermann K, Stuart M, Wex C, Protzer U, Schatzl HM, and Gilch S (2012). Severe acute respiratory syndrome coronavirus replication is severely impaired by MG132 due to proteasome-independent inhibition of M-calpain. J Virol 86, 10112–10122. [PubMed: 22787216]

Schneider WM, Luna JM, Hoffmann HH, Sanchez-Rivera FJ, Leal AA, Ashbrook AW, Le Pen J, Ricardo-Lax I, Michailidis E, Peace A, et al. (2021). Genome-Scale Identification of SARS-CoV-2 and Pan-coronavirus Host Factor Networks. Cell 184, 120–132 e114. [PubMed: 33382968]

Sclip A, Bacaj T, Giam LR, and Sudhof TC (2016). Extended Synaptotagmin (ESyt) Triple Knock-Out Mice Are Viable and Fertile without Obvious Endoplasmic Reticulum Dysfunction. PLoS One 11, e0158295. [PubMed: 27348751]

Shi X, Yokom AL, Wang C, Young LN, Youle RJ, and Hurley JH (2020). ULK complex organization in autophagy by a C-shaped FIP200 N-terminal domain dimer. J Cell Biol 219.

Snijder EJ, Limpens R, de Wilde AH, de Jong AWM, Zevenhoven-Dobbe JC, Maier HJ, Faas F, Koster AJ, and Barcena M (2020). A unifying structural and functional model of the coronavirus

replication organelle: Tracking down RNA synthesis. PLoS Biol 18, e3000715. [PubMed: 32511245]

Snijder EJ, van der Meer Y, Zevenhoven-Dobbe J, Onderwater JJ, van der Meulen J, Koerten HK, and Mommaas AM (2006). Ultrastructure and origin of membrane vesicles associated with the severe acute respiratory syndrome coronavirus replication complex. J Virol 80, 5927–5940. [PubMed: 16731931]

Sola I, Almazan F, Zuniga S, and Enjuanes L (2015). Continuous and Discontinuous RNA Synthesis in Coronaviruses. Annu Rev Virol 2, 265–288. [PubMed: 26958916]

Soreng K, Munson MJ, Lamb CA, Bjorndal GT, Pankiv S, Carlsson SR, Tooze SA, and Simonsen A (2018). SNX18 regulates ATG9A trafficking from recycling endosomes by recruiting Dynamin-2. EMBO Rep.

Strating JR, and van Kuppeveld FJ (2017). Viral rewiring of cellular lipid metabolism to create membranous replication compartments. Curr Opin Cell Biol 47, 24–33. [PubMed: 28242560]

Stukalov A, Girault V, Grass V, Bergant V, Karayel O, Urban C, Haas DA, Huang Y, Oubraham L, Wang A, et al. (2020). Wang, et al. 2020. Multi-level proteomics reveals host-perturbation strategies of SARS-CoV-2 and SARS-CoV. . bioRxiv.

Sugo M, Kimura H, Arasaki K, Amemiya T, Hirota N, Dohmae N, Imai Y, Inoshita T, Shiba-Fukushima K, Hattori N, et al. (2018). Syntaxin 17 regulates the localization and function of PGAM5 in mitochondrial division and mitophagy. EMBO J.

Szalai P, Hagen LK, Saetre F, Luhr M, Sponheim M, Overbye A, Mills IG, Seglen PO, and Engedal N (2015). Autophagic bulk sequestration of cytosolic cargo is independent of LC3, but requires GABARAPs. Exp Cell Res 333, 21–38. [PubMed: 25684710]

Takahashi Y, He H, Tang Z, Hattori T, Liu Y, Young MM, Serfass JM, Chen L, Gebru M, Chen C, et al. (2018). An autophagy assay reveals the ESCRT-III component CHMP2A as a regulator of phagophore closure. Nature communications 9, 2855.

Takats S, Glatz G, Szenci G, Boda A, Horvath GV, Hegedus K, Kovacs AL, and Juhasz G (2018). Non-canonical role of the SNARE protein Ykt6 in autophagosome-lysosome fusion. PLoS Genet 14, e1007359. [PubMed: 29694367]

Takats S, Nagy P, Varga A, Pircs K, Karpati M, Varga K, Kovacs AL, Hegedus K, and Juhasz G (2013). Autophagosomal Syntaxin17-dependent lysosomal degradation maintains neuronal function in Drosophila. J Cell Biol 201, 531–539. [PubMed: 23671310]

Tanaka Y, Guhde G, Suter A, Eskelinen EL, Hartmann D, Lullmann-Rauch R, Janssen PM, Blanz J, von Figura K., and Saftig P (2000). Accumulation of autophagic vacuoles and cardiomyopathy in LAMP-2-deficient mice. Nature 406, 902–906. [PubMed: 10972293]

Teis D, Saksena S, and Emr SD (2008). Ordered assembly of the ESCRT-III complex on endosomes is required to sequester cargo during MVB formation. Dev Cell 15, 578–589. [PubMed: 18854142]

Tesei A, Cortesi M, Zamagni A, Arienti C, Pignatta S, Zanoni M, Paolillo M, Curti D, Rui M, Rossi D, et al. (2018). Sigma Receptors as Endoplasmic Reticulum Stress "Gatekeepers" and their Modulators as Emerging New Weapons in the Fight Against Cancer. Front Pharmacol 9, 711. [PubMed: 30042674]

Thurston TL, Ryzhakov G, Bloor S, von Muhlinen N, and Randow F (2009). The TBK1 adaptor and autophagy receptor NDP52 restricts the proliferation of ubiquitin-coated bacteria. Nat Immunol 10, 1215–1221. [PubMed: 19820708]

Tooze SA, and Yoshimori T (2010). The origin of the autophagosomal membrane. Nat Cell Biol 12, 831–835. [PubMed: 20811355]

Travassos LH, Carneiro LA, Ramjeet M, Hussey S, Kim YG, Magalhaes JG, Yuan L, Soares F, Chea E, Le Bourhis L, et al. (2010). Nod1 and Nod2 direct autophagy by recruiting ATG16L1 to the plasma membrane at the site of bacterial entry. Nature immunology 11, 55–62. [PubMed: 19898471]

Vandecaetsbeek I, Vangheluwe P, Raeymaekers L, Wuytack F, and Vanoevelen J (2011). The Ca2+ pumps of the endoplasmic reticulum and Golgi apparatus. Cold Spring Harb Perspect Biol 3.

Vargas JNS, Wang C, Bunker E, Hao L, Maric D, Schiavo G, Randow F, and Youle RJ (2019). Spatiotemporal Control of ULK1 Activation by NDP52 and TBK1 during Selective Autophagy. Mol Cell 74, 347–362 e346. [PubMed: 30853401]

Velikkakath AK, Nishimura T, Oita E, Ishihara N, and Mizushima N (2012). Mammalian Atg2 proteins are essential for autophagosome formation and important for regulation of size and distribution of lipid droplets. Molecular biology of the cell 23, 896–909. [PubMed: 22219374]

Vilner BJ, John CS, and Bowen WD (1995). Sigma-1 and sigma-2 receptors are expressed in a wide variety of human and rodent tumor cell lines. Cancer Res 55, 408–413. [PubMed: 7812973]

Violot S, Carpentier P, Blanchoin L, and Bourgeois D (2009). Reverse pH-dependence of chromophore protonation explains the large Stokes shift of the red fluorescent protein mKeima. J Am Chem Soc 131, 10356–10357. [PubMed: 19722611]

Vollrath JT, Sechi A, Dreser A, Katona I, Wiemuth D, Vervoorts J, Dohmen M, Chandrasekar A, Prause J, Brauers E, et al. (2014). Loss of function of the ALS protein SigR1 leads to ER pathology associated with defective autophagy and lipid raft disturbances. Cell Death Dis 5, e1290. [PubMed: 24922074]

Wang L, Kim JY, Liu HM, Lai MMC, and Ou JJ (2017). HCV-induced autophagosomes are generated via homotypic fusion of phagophores that mediate HCV RNA replication. PLoS Pathog 13, e1006609. [PubMed: 28931085]

Wang Z, Miao G, Xue X, Guo X, Yuan C, Wang Z, Zhang G, Chen Y, Feng D, Hu J, et al. (2016). The Vici Syndrome Protein EPG5 Is a Rab7 Effector that Determines the Fusion Specificity of Autophagosomes with Late Endosomes/Lysosomes. Mol Cell 63, 781–795. [PubMed: 27588602]

Watanabe S, Ilieva H, Tamada H, Nomura H, Komine O, Endo F, Jin S, Mancias P, Kiyama H, and Yamanaka K (2016). Mitochondria-associated membrane collapse is a common pathomechanism in SIGMAR1- and SOD1-linked ALS. EMBO Mol Med 8, 1421–1437. [PubMed: 27821430]

Wild P, Farhan H, McEwan DG, Wagner S, Rogov VV, Brady NR, Richter B, Korac J, Waidmann O, Choudhary C, et al. (2011). Phosphorylation of the autophagy receptor optineurin restricts Salmonella growth. Science 333, 228–233. [PubMed: 21617041]

Wolff G, Limpens R, Zevenhoven-Dobbe JC, Laugks U, Zheng S, de Jong AWM, Koning RI, Agard DA, Grunewald K, Koster AJ, et al. (2020). A molecular pore spans the double membrane of the coronavirus replication organelle. Science 369, 1395–1398. [PubMed: 32763915]

Wyant GA, Abu-Remaileh M, Frenkel EM, Laqtom NN, Dharamdasani V, Lewis CA, Chan SH, Heinze I, Ori A, and Sabatini DM (2018). NUFIP1 is a ribosome receptor for starvation-induced ribophagy. Science 360, 751–758. [PubMed: 29700228]

Yang H, Shen H, Li J, and Guo LW (2019). SIGMAR1/Sigma-1 receptor ablation impairs autophagosome clearance. Autophagy 15, 1539–1557. [PubMed: 30871407]

Youle RJ (2019). Mitochondria-Striking a balance between host and endosymbiont. Science 365.

Zechner R, Madeo F, and Kratky D (2017). Cytosolic lipolysis and lipophagy: two sides of the same coin. Nat Rev Mol Cell Biol 18, 671–684. [PubMed: 28852221]

Zhao YG, Chen Y, Miao G, Zhao H, Qu W, Li D, Wang Z, Liu N, Li L, Chen S, et al. (2017). The ER-Localized Transmembrane Protein EPG-3/VMP1 Regulates SERCA Activity to Control ER-Isolation Membrane Contacts for Autophagosome Formation. Mol Cell 67, 974–989 e976. [PubMed: 28890335]

Zhao Z, Thackray LB, Miller BC, Lynn TM, Becker MM, Ward E, Mizushima NN, Denison MR, and Virgin H.W.t. (2007). Coronavirus replication does not require the autophagy gene ATG5. Autophagy 3, 581–585. [PubMed: 17700057]

Zhen Y, Spangenberg H, Munson MJ, Brech A, Schink KO, Tan KW, Sorensen V, Wenzel EM, Radulovic M, Engedal N, et al. (2020). ESCRT-mediated phagophore sealing during mitophagy. Autophagy 16, 826–841. [PubMed: 31366282]

Zhou P, Yang XL, Wang XG, Hu B, Zhang L, Zhang W, Si HR, Zhu Y, Li B, Huang CL, et al. (2020). A pneumonia outbreak associated with a new coronavirus of probable bat origin. Nature 579, 270–273. [PubMed: 32015507]

Zhu L, Mou C, Yang X, Lin J, and Yang Q (2016). Mitophagy in TGEV infection counteracts oxidative stress and apoptosis. Oncotarget 7, 27122–27141. [PubMed: 27027356]

Highlights

i. Mammalian autophagosomes are formed via fusion of cis-Golgi and endosomal membranes

ii. This forms a prophagophore termed Hybrid Pre-Autophagosomal Structure (HyPAS)

iii. HyPAS depends on SNARE STX17 and its interactors E-SYT2, SIGMAR1 and SERCA2

iv. SARS-CoV-2 inhibits prophagophore formation by nsp6 targeting HyPAS apparatus
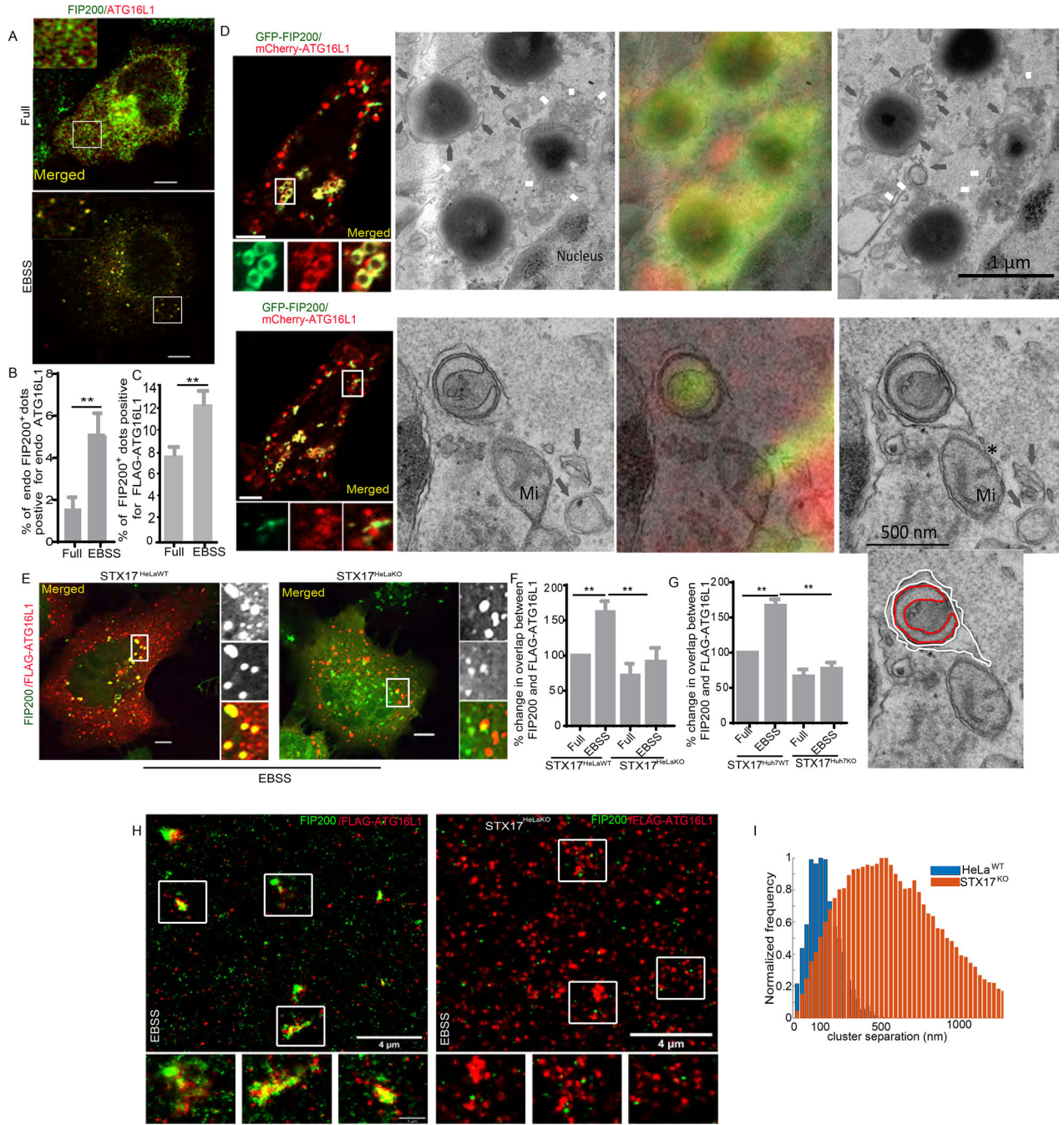
Figure 1. STX17 is required for colocalization between FIP200 and ATG16L1
(**A**) Effects of autophagy induction (EBSS 2h) on colocalization (confocal microscopy) between endogenous FIP200 and ATG16L1 in HeLa cells. Scale bar, 5 μm. (**B**) HCM quantification of colocalization between endogenous FIP200 and ATG16L1 in HeLa cells. (**C**) HCM quantification of colocalization between FIP200 and FLAG-ATG16L1 in HeLa cells. B and C, **, p < 0.01, (n=3) t-test. (**D**) (**i-iii**) CLEM of HeLa cells expressing GFP-FIP200 and mCherry-ATG16L1. Boxed area (panel i) is shown at TEM level in panels ii-iii, representing two Z sections 70 nm apart. Panel ii', overlay of fluorescence and

TEM. Yellow fluorescence in panel a corresponds to vesicular (white arrows) and tubular (gray arrows) elements in TEM. Asterisk, a small double-membrane structure or a cross-section of a cup-shaped cisternal element. White asterisks (panels (v and v') correspond to phagophore membrane. Black asterisk (panel vi), ER-mitochondrial contact site. The membranes of the phagophore (red) and ER surrounding it (white) are traced in panel vii. Nu, nucleus, Mi, mitochondrion. Scale bar in (i) and (iv) 5 μm. **(E)** Effect of STX17 KO on colocalization (confocal microscopy) between endogenous FIP200 and FLAG-ATG16L1 in HeLa cells induced for autophagy (EBSS, 2h). Scale bar, 5 μm. **(F,G)** STX17 KO effects on colocalization between FIP200 and FLAG-ATG16L1 in HeLa and Huh7 cells (HCM). **, $p < 0.01$, (n=3) ANOVA. **(H,I)** Super-resolution microscopy and cluster analysis of FLAG-ATG16L1 and endogenous FIP200 in HeLa^{WT} or STX17^{KO} cells incubated with EBSS for 2h. See also Figures S1 and S2.
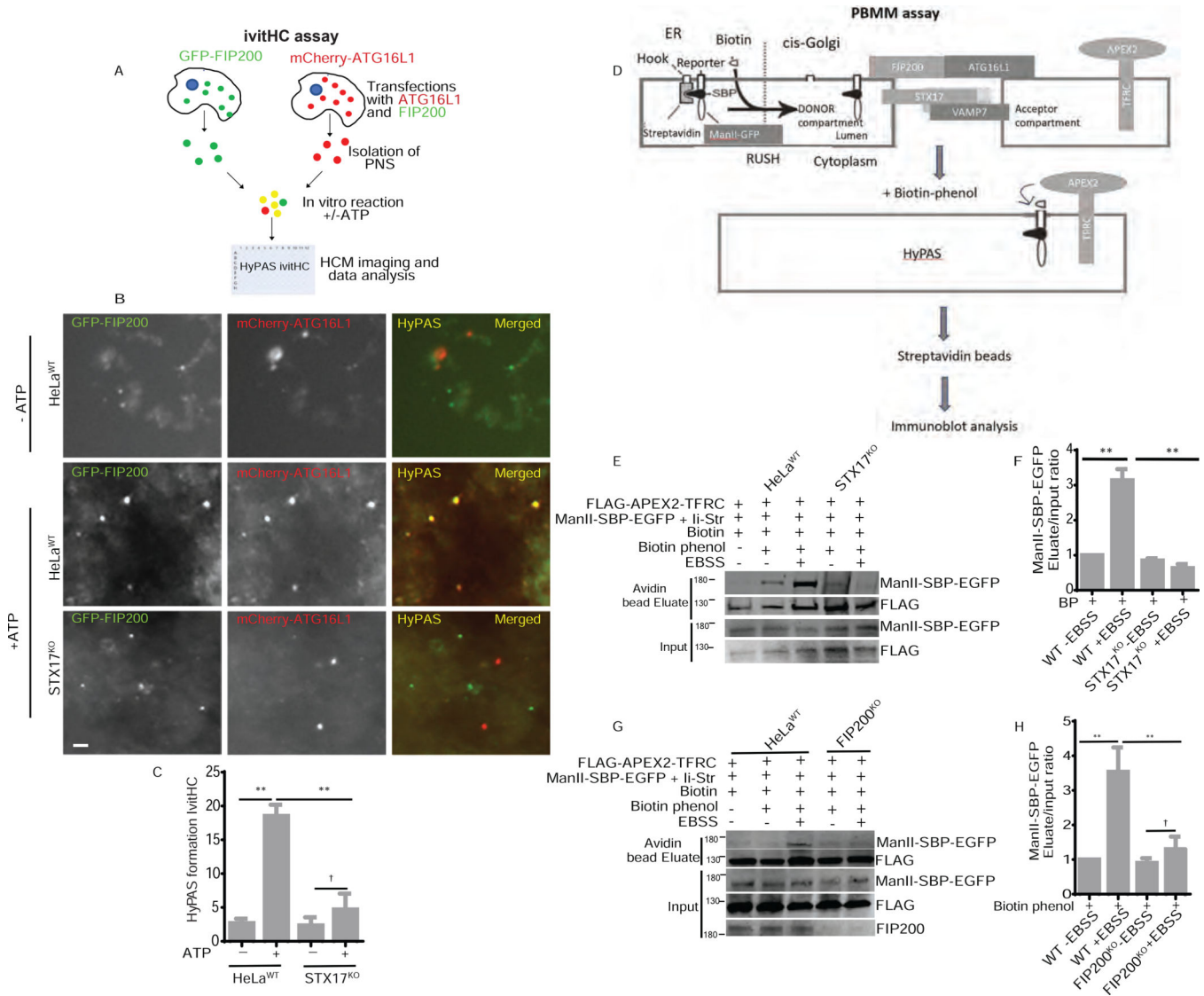
Figure 2. STX17 is required for HyPAS formation.
(A) Schematic of in vitro fusion assay (ivitHC) between GFP-FIP200 and mCherry-ATG16L1 compartments utilizing high content microscopy quantification. **(B,C)** Quantification of the effects of STX17 KO on HyPAS formation in vitro (IvitHC). Scale bar 500nm. **(D)** PBMM assay (schematic) is a combination of RUSH and APEX-2 proximity biotinylation. **(E-H)** PBMM quantification of the effects of STX17 KO and FIP200 KO on starvation-induced mixing of early/cis-Golgi (ManII) and endosomal (TFRC) compartments. † p 0.05, **, p < 0.01, (n=3) ANOVA. See also Figures S2 and S3.
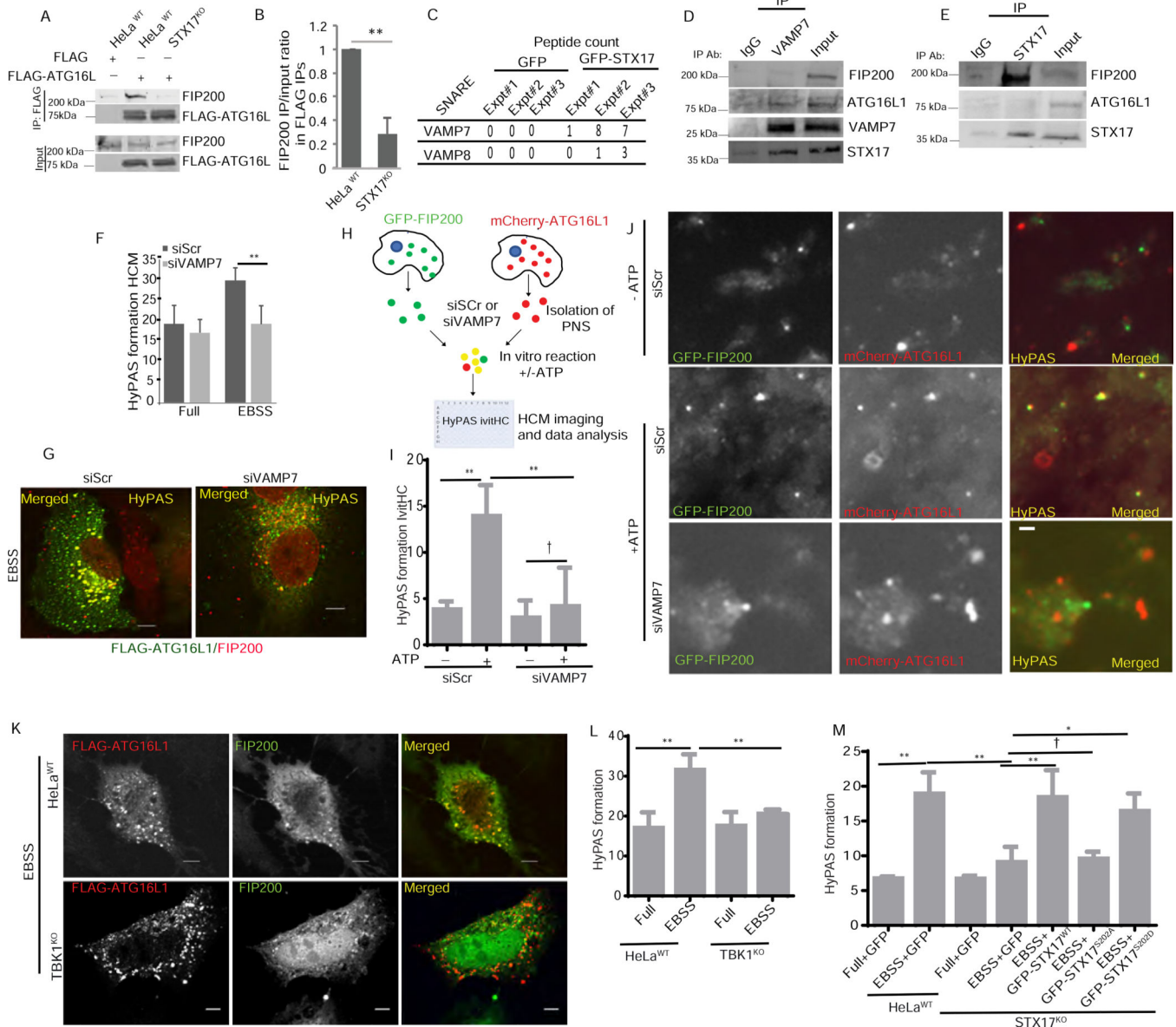
Figure 3. STX17 is required for association between FIP200 and ATG16L1.
(A,B) Co-IP analysis and quantifications of FIP200 and FLAG-ATG16L1 interactions in WT or STX17[KO] HeLa cells. **, $p < 0.01$, (n=3) t-test. **(C)** MS analysis, GFP vs. GFP-STX17 peptides in VAMP7 complexes. **(D,E)** Co-IP analysis of interactions between endogenous proteins: VAMP7 or STX17, with ATG16L1 or FIP200. **(F)** Effects of VAMP7 KD on colocalization between FIP200 and FLAG-ATG16L1 in HeLa cells (HCM quantification). Y-axis, % of FIP200^{+} profiles that were also ATG16L1[+] (a measure of HyPAS). **, $p < 0.01$, (n=3) ANOVA. **(G)** Effect of VAMP7 KD on HyPAS formation (confocal microscopy) in HeLa cells induced for autophagy (EBSS, 2h). Scale bar, 5 μm. Individual channels related to this panel are shown in Figure S3U. **(H-J)** ivitHC schematic, quantification, and images of VAMP7 KD effect on HyPAS formation in vitro. Vesicle source cells were induced for autophagy by incubating in EBSS for 2h. † p 0.05, **, p

< 0.01, (n=3) ANOVA. Scale bar 500nm. **(K)** Effects of TBK1 KO on HyPAS formation (confocal microscopy) in cells induced for autophagy (EBSS; 2h). Scale bar, 5 μm. **(L)** HCM quantification of the effects of TBK1 KO on HyPAS formation. **, $p < 0.01$, (n=3) ANOVA. **(M)** Complementation analysis (HyPAS quantification by HCM): STX17 KO cells transfected with GFP fusions with STX17 wild type, non-phosphorylatable mutant of STX17 (S202A) or phosphomimetic mutant of STX17 (S202D). † p 0.05, **, $p < 0.01$, (n=3) ANOVA. See also Figures S3 and S4.
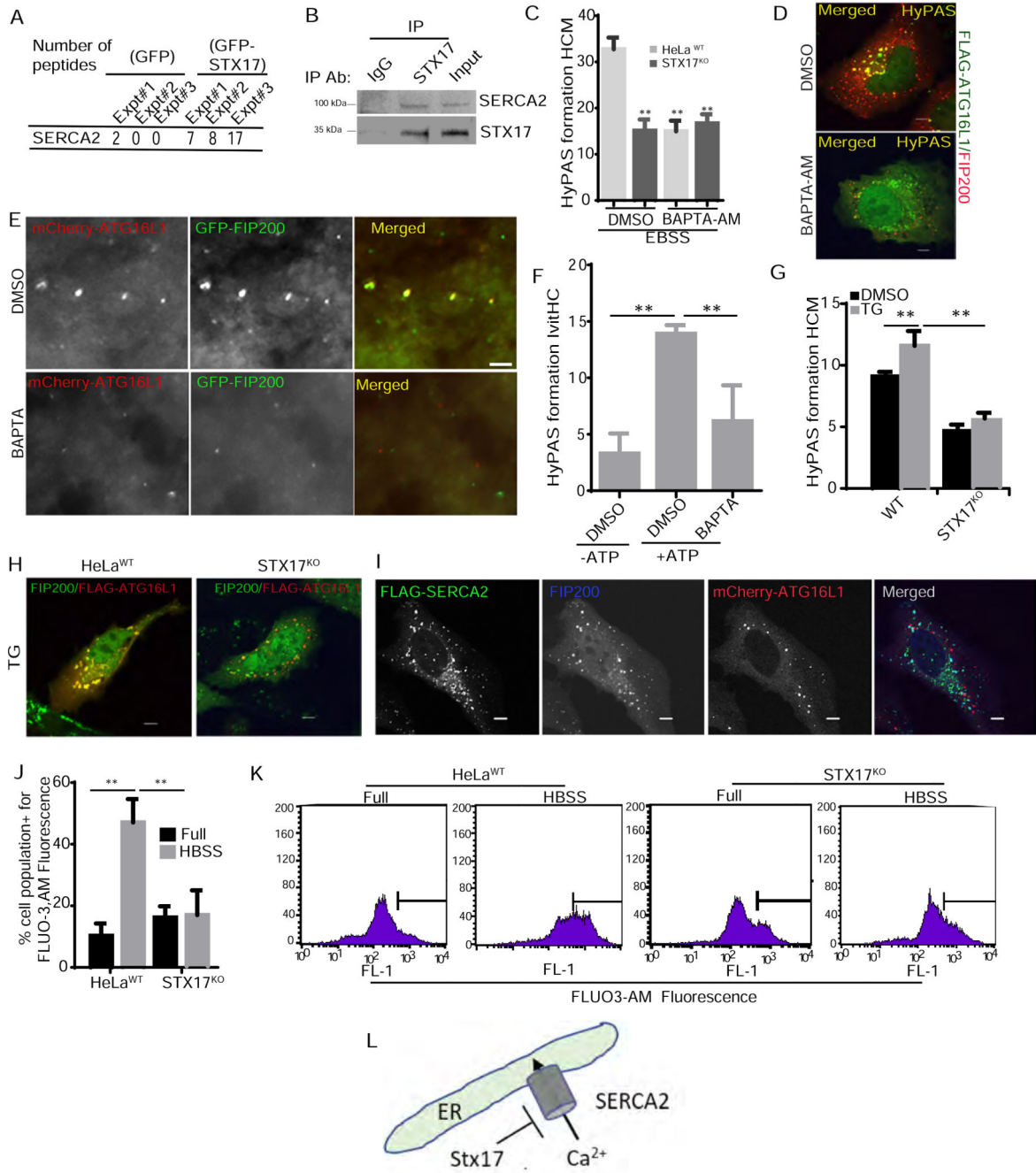
Figure 4. Ca2+ positively regulates HyPAS formation.
(**A**) SERCA2 peptides (MS analysis) in GFP or GFP-STX17 complexes. (**B**) Co-IP analysis with GFP-STX17 and endogenous SERCA2. (**C,D**) Effects (C, HCM; D, confocal microscopy) of BAPTA-AM treatment on HyPAS formation in WT and STX17[KO] HeLa cells, **, p < 0.01, (n=3) ANOVA. Scale bar, 5 μm. (**E,F**) Effect of BAPTA on HyPAS formation in vitro (IvitHC assay) in cells induced for autophagy. **, p < 0.01, (n=3) ANOVA. Scale bar, 1 μm. (**G**) Effect of thapsigargin treatment on HyPAS formation in WT and STX17[KO] HeLa cells (HCM). **, p < 0.01, (n=3) ANOVA. (**H**) Confocal microscopy

images of the effect of thapsigargin treatment on HyPAS formation in WT and STX17^{KO} HeLa cells. Scale bar, 5 μm. **(I)** Confocal microscopy analysis of colocalization between FLAG-SERCA2, FIP200 and mCherry-ATG16L1 in HeLa cells induced for autophagy (EBSS, 2h). Scale bar, 5 μm. **(J,K)** Flow cytometry analysis of the effect of STX17 KO on FLUO-3AM fluorescence in cells incubated in full media or in HBSS for 4h. **, $p < 0.01$, (n=3) ANOVA. **(L)** A schematic representation of the effect of STX17 on SERCA2 and Ca^{2+} flow from cytosol to ER lumen. See also Figure S4.
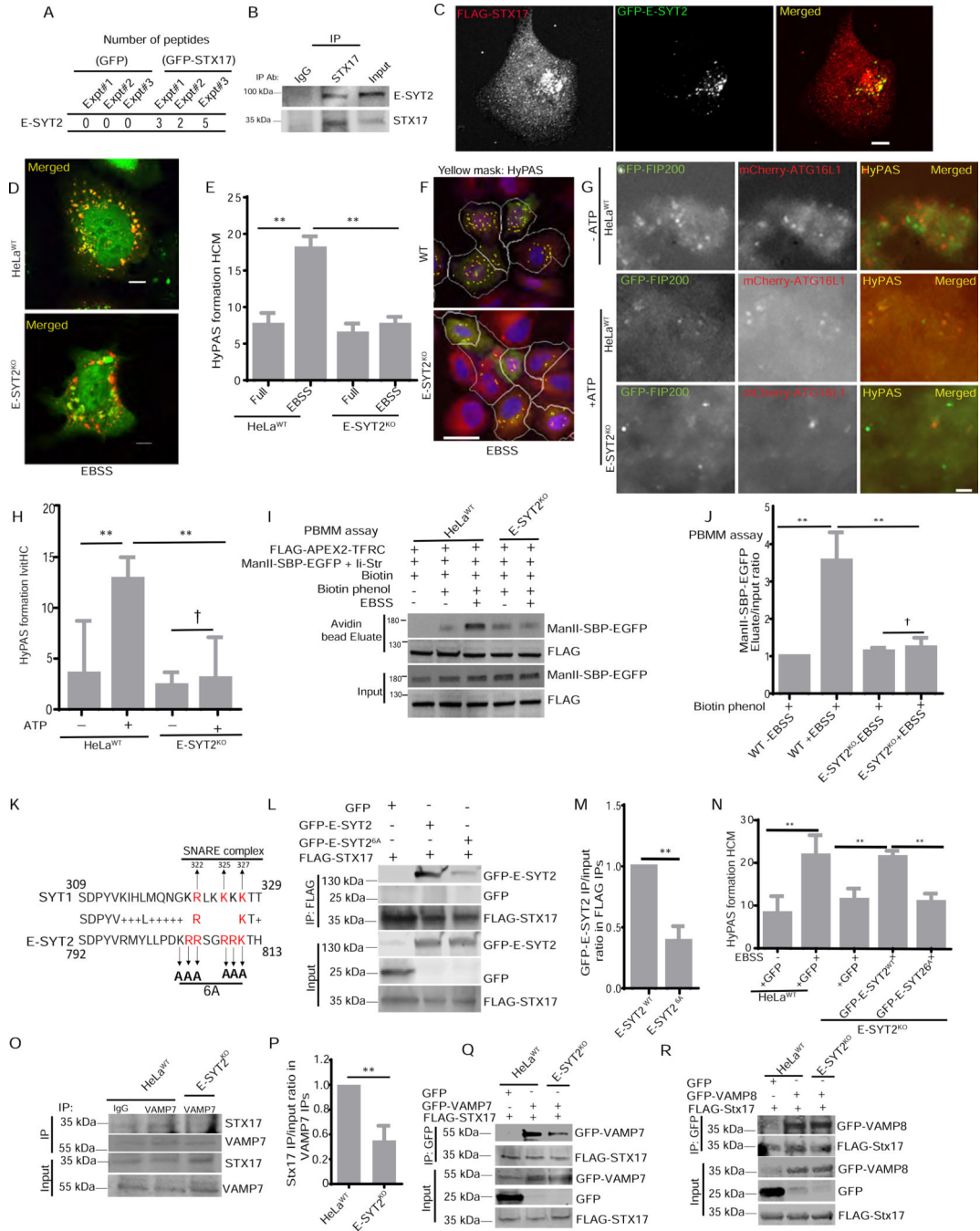
Figure 5. STX17 interactor E-SYT2 controls HyPAS formation.
(**A**) E-SYT2 peptides (MS analysis) in GFP or GFP-STX17 complexes. (**B**) Co-IP analysis, endogenous STX17 and E-SYT2. (**C**) Localization (confocal microscopy) of GFP-E-SYT2 and FLAG-STX17 in HeLa cells. Scale bar, 5 μm**. (D)** Effect of E-SYT2 KO on HyPAS formation (confocal microscopy) in HeLa induced for autophagy (EBSS, 2h). Scale bar, 5 μm. (**E,F**) HCM quantification of HyPAS formation in WT or E-SYT2^{KO} HeLa. Masks: white, primary objects (FLAG positive cells), yellow puncta, overlap between FIP200 and FLAG-ATG16L1. **, p < 0.01, (n=3) ANOVA. Scale bar, 10 μm. (**G,H**) In vitro HyPAS

formation, effect of E-SYT2 KO (ivitHC quantification). Fusing vesicle preparations were from cells induced for autophagy (EBSS for 2h). † p 0.05, **, p < 0.01, (n=3) ANOVA. **(I,J)** PBMM assay and quantifications of the effects of E-SYT2 KO on starvation-induced membrane mixing. The experimental conditions were same as in Figure 2E,F. † p 0.05, **, p < 0.01, (n=3) ANOVA. **(K)** Alignment of conserved residues in the polybasic regions of Synaptotagmin 1 and E-SYT2. Upward arrows, key residues in SNARE interactions; downward arrows, basic residues mutated to Ala in E-SYT2[6A]. **(L,M)** Co-IP analysis, GFP-E-SYT2 WT or GFP-E-SYT2[6A] with FLAG-STX17. p>0.05; ** p < 0.01, (n=3) t-test. **(N)** Complementation of E-SYT2 KO with WT or E-SYT2[6A]; HCM analysis of HyPAS formation, † p 0.05, **, p < 0.01, (n=3) ANOVA. **(O,P)** Co-IP, STX17 and VAMP7 in WT or E-SYT2[KO] HeLa. **, p < 0.01, (n=3) t-test. **(Q)** Co-IP, FLAG-STX17 and GFP-VAMP7 in WT or E-SYT2[KO] HeLa. **(R)** Co-IP, FLAG-STX17 and GFP-VAMP8 in WT or E-SYT2[KO] HeLa. See also Figure S5.
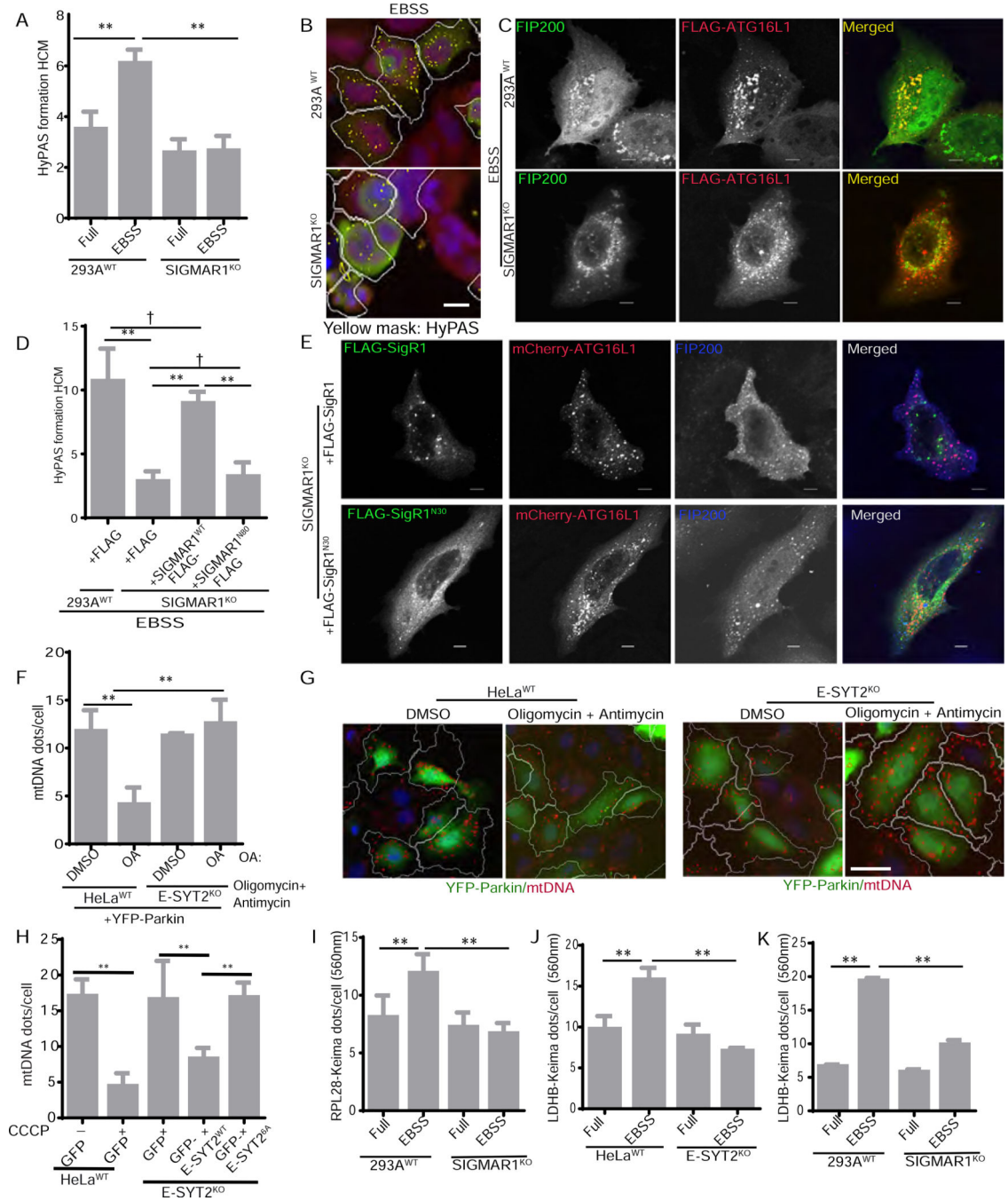
Figure 6. SIGMAR1 is required for HyPAS formation and HyPAS apparatus affects autophagy of diverse cargo.

(**A,B**) Effect (HCM quantification) of SIGMAR1 KO on HyPAS formation in 293A cells. Masks: white, primary objects (FLAG positive cells), yellow puncta, overlap between FIP200 and FLAG-ATG16L1. Scale bar, 5 μm. (**C**) Confocal microscopy of HyPAS in WT or SIGMAR1^KO 293A cells. Scale bar, 5 μm. (**D**) Effect of complementation of SIGMAR1 KO with empty FLAG, SIGMAR1-FLAG or with SIGMAR1 N80-FLAG. on HyPAS formation in SIGMAR1^KO 293A cells. HCM quantification. (**E**) Confocal microscopy

images related to D. Scale bar, 5 μm. **(F,G)** Effect of E-SYT2 KO on mitophagy induced by OA (oligomycin+antimycin) treatment. Cells were transfected with YFP-Parkin. YFP-Parkin positive cells were gated for HCM quantification of mito-DNA dots (mitophagy). Masks: white, primary objects (YFP-Parkin positive cells), red puncta, mito-DNA dots. **(H)** Complementation of E-SYT2 KO with WT or E-SYT2^{6A} in mitophagy assayed by mtDNA clearance (HCM quantifications) in mCherry-Parkin^{+} cells. Masks: white, primary objects (GFP and mCherry positive cells), blue puncta, mtDNA dots. **(I)** Effect of SIGMAR1 KO on ribophagy using RPL28-Keima probe (HCM quantification). **(J,K)** Effect of E-SYT2 KO or SIGMAR1 KO on bulk autophagy using LDH-Keima probe (HCM quantification). All graphs, †, $p>0.05$; **, $p < 0.01$, (n=3) ANOVA. See also Figure S6.
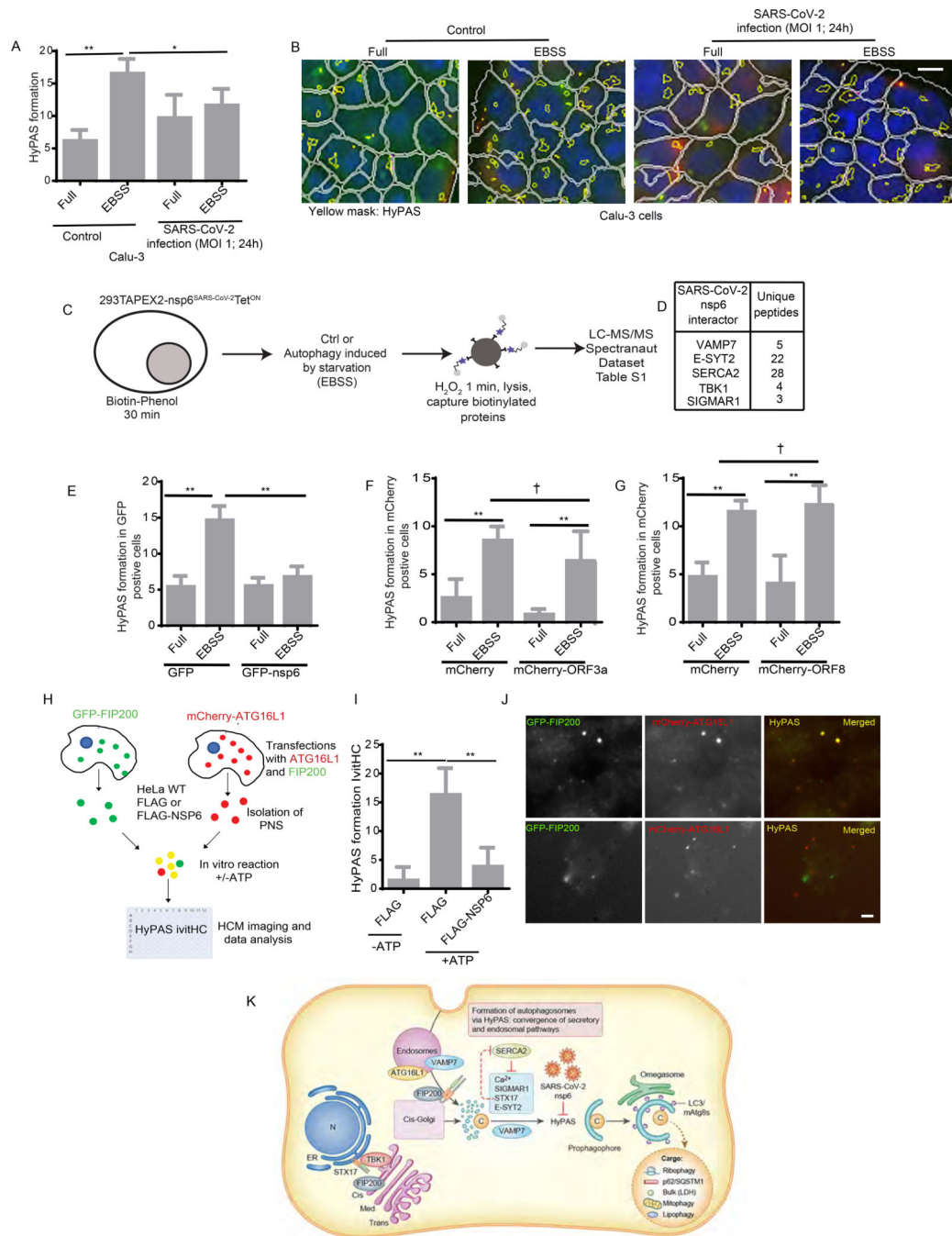
Figure 7. HyPAS is inhibited in cells infected with SARS-CoV-2 and SARS-CoV-2 nsp6 inhibits HyPAS.

(A,B) Effects of SARS-CoV-2 infection (MOI: 1, 24h) on HyPAS formation in Calu-3 cells; HCM quantification. Masks: white, primary objects (FLAG positive cells), yellow puncta, HyPAS. Scale bar, 10 μm. **(C,D)** Proximity biotinylation proteomics using 293T-APEX2-nsp6Tet[ON] cells. Table, subset of SARS-CoV-2-nsp6 interactors; full proteomics data in Table S1. **(E-G)** Effects (HCM quantification) on HyPAS formation of GFP-nsp6, mChery-ORF3a and mCherry-ORF8 expression. **(H-J)** Quantification (ivitHC) of the effects

of FLAG-nsp6 on HyPAS formation in the vitro fusion assay. Source cells were induced for autophagy (EBSS for 2h). Scale bar, 0.5 μm. All graphs, † p ⩽ 0.05, **, p < 0.01, (n=3) ANOVA. **(K)** Schematic, HyPAS prophagophore formation and the canonical autophagy pathway. HyPAS is generated through a regulated fusion of vesicles and cisternae derived from the early secretory and endosomal pathways to form a prophagophore, which progresses to an LC3-positive phagophore closing to sequester cargo (C) destined for degradation. SARS-CoV-2 infection and at least one of SARS-CoV-2 proteins, nsp6, inhibit HyPAS formation. See also Figure S7 and Table S1.